Modelling the response of systems for detection of nuclear explosions and other nuclear events

PETER JANSSON, SOFIE LILJEGREN, ANDERS RINGBOM,
PER ANDERSSON, OSCAR BJÖRNHAM, JON GRUMER,
LEIF Å PERSSON, DANIEL VÅGBERG

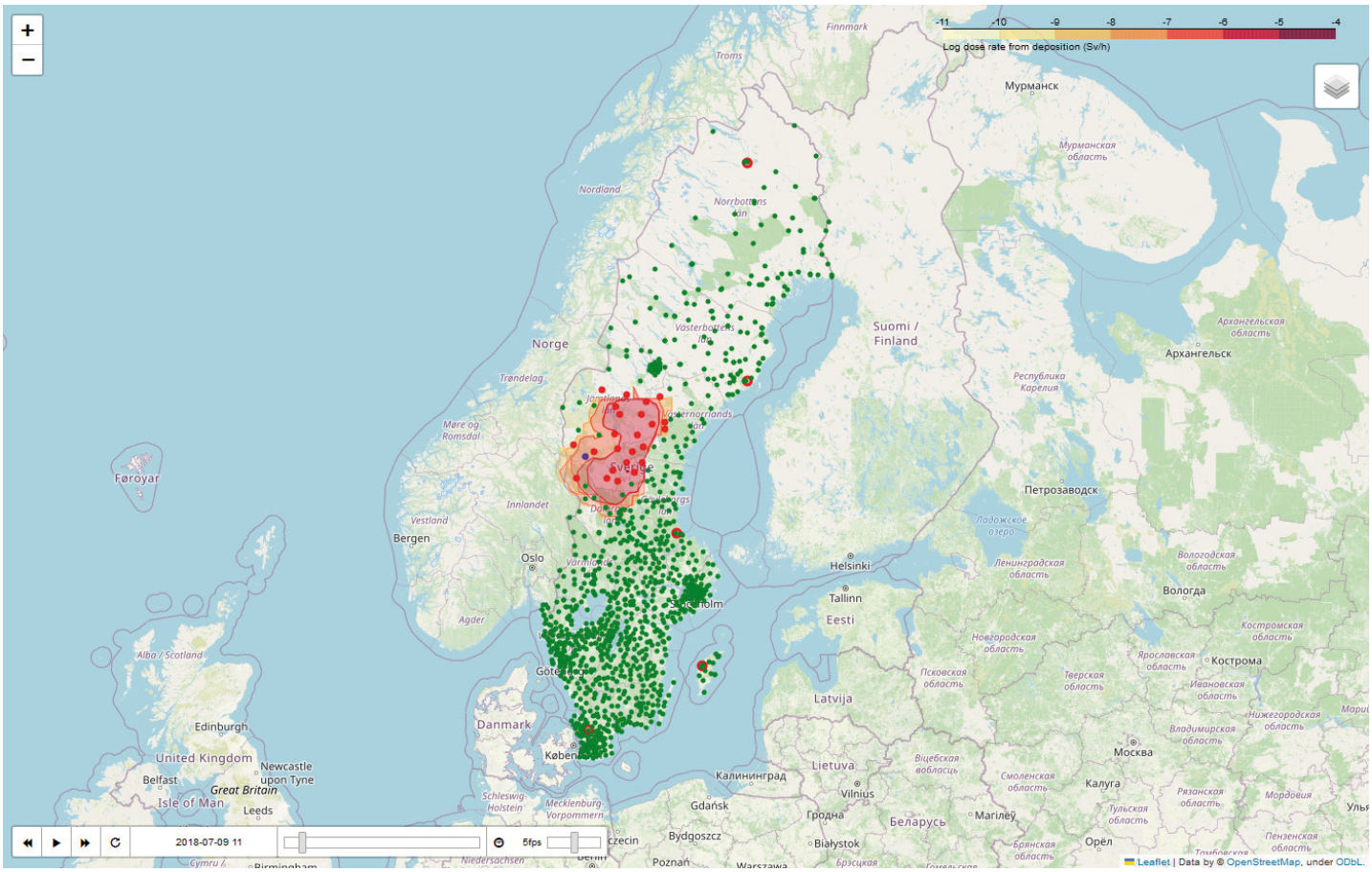

FOI-R--5626--SE
ISSN 1650-1942 June 2024

Peter Jansson, Sofie Liljegren, Anders Ringbom, Per Andersson, Oscar Björnham, Jon Grumer, Leif Å Persson, Daniel Vågberg

Modelling the response of systems for detection of nuclear explosions and other nuclear events.

An example of a map showing the dose rate from ground deposition a few hours following a hypothetical nuclear explosion in Sweden. The green and red markers indicate dose rate measurement positions. Larger red circles indicate aerosol sampling stations detecting the release. The blue marker is ground zero.

Titel	Att modellera responsen från ett system för detektion av kärnexplosioner och andra nukleära händelser.
Title	Modelling the response of systems for detection of nuclear explosions and other nuclear events.
Report no	FOI-R--5626--SE
Month	June
Year	2024
Pages	77
ISSN	ISSN-1650-1942
Customer	Swedish Civil Contingencies Agency (MSB)
Project no	B402423
Approved by	Niklas Brännström
Division	CBRN Defence and Security
FOI Research area	CBRN issues and non-proliferation

Abstract

This report describes methodology and functionality of a software framework (NEMOS - Nuclear Event Monitoring Simulator) developed to simulate the response of sensor networks, which are intended to detect, identify, and locate nuclear explosions and other nuclear events. The Python-based software simulates the response of networks that can consist of seismic sensors, infrasound detection sensors, and several types of radioactivity instruments (GM - tubes measuring dose rate, NaI- sensors measuring isotope-specific activity; either stand-alone or in the vicinity of an air sampling filter; aerosol stations equipped with an HPGe detector, and finally, two types of radioxenon measurement systems).

NEMOS use a nuclear source vector and atmospheric transport calculations in combination with various detector response models to simulate the radioactivity measurements. A nuclear explosion source vector has been developed that takes into account fission products and neutron activation in weapon material as well as in surrounding media.

In the case of HPGe and NaI measurements, a full simulation of measured spectra is performed. HPGe spectra are analysed with respect to nuclide specific activities and activity concentrations using standard radionuclide analysis software, and NaI data is treated using a more basic technique. The responses (detection capability and location accuracy) of the seismic and infrasound sensors are calculated using empirical models.

A large number of nuclear explosions located in and around Sweden, as well as in Europe, were simulated with respect to atmospheric dispersion of aerosols and noble gases. Network responses from these explosions can be used in a statistical analysis designed to evaluate different network configurations with respect to verification capability. The analysis include calculation of parameters such as reporting time, detection and location capability, and the capability to identify whether an explosion is nuclear in nature or not.

The framework can also be used to produce interactive maps that show the calculated dispersion fields and which sensors in the network that are detecting the event. The maps also show detailed measurement data from the individual sensors. In addition, direct effects can be illustrated. The maps, which can be viewed in any web browser, can also be useful when planning and conducting exercises, as well as in general discussions on nuclear weapons effects.

Keywords

FOI, nuclear explosion detection, seismic network, infrasound, airborne radioactivity, radioxenon, atmospheric transport modelling

Sammanfattning

Denna rapport beskriver metodologi och funktionalitet för en mjukvara (NEMOS - Nuclear Event Monitoring Simulator) som utvecklats med syftet att simulera responsen för sensornätverk avsedda för att detektera, identifiera och lokalisera kärnexplosioner och andra nukleära händelser. Den Python-baserade mjukvaran simulerar responsen från nätverk som i sin tur kan bestå av ett seismiskt nätverk, ett nätverk för infraljudsmätningar, samt flera typer av sensorer för radioaktivitet (GM- rör som mäter dosrat, NaI-detektorer som mäter isotopspecifik aktivitet, antingen i anslutning till ett partikelfilter för luftinsamling eller i luften, aerosolstationer utrustade med HPGe-detektorer, samt två typer av system för mätning av radioaktivt xenon).
NEMOS använder sig av en nuklidvektor och atmosfärstransportberäkningar i kombination med detektorresponsmodeller för att simulera mätningar i nätverket. En nuklidvektor för fallet kärnexplosion har utvecklats som tar hänsyn till fissionsprodukter och neutronaktivering i vapenmaterial och omgivande media. För HPGe- och NaI-detektorer utförs en komplett simulering av uppmätta spektra. HPGe-spektra analyseras sedan med standardprogram för radionuklidanalys, medan NaI-spektra analyseras med en enklare metod. Responsen för seismik och infraljud beräknas med empiriska modeller.
Ett stort antal kärnexplosioner i Sverige och dess närområde har simulerats både med avseende på spridning av aerosoler och ädelgaser. Simulerade nätverksresponser kan sedan användas i en statistisk analys utformad för att utvärdera olika nätverkskonfigurationer med avseende på verifikationsförmåga. Analysen inkluderar beräkningar av parametrar som rapporeringstingstid, detektions- och lokaliseringsförmåga, samt kapacitet att identifiera kärnexplosioner.
Mjukvaran kan även användas för att producera interaktiva web-baserade kartor som visar de beräknade spridningsfälten och vilka sensorer som detekterar signaler från händelsen. Kartorna visar även detaljerade data från individuella sensorer. Dessutom kan direkta effekter illustreras. Kartorna kan även vara användbara vid planering och genomförande av övningar, och vid generella diskussioner rörande effekter från kärnexplosioner.

Nyckelord

FOI, detektion av kärnexplosioner, seismiska nätverk, infraljud, luftburen radioaktivitet, radioxenon, modellering av atmosfärstransport

Contents

1 Introduction

This report contains a description of the methodology for a software framework developed to simulate the response of sensor networks which are intended to detect, identify, and locate nuclear explosions and other nuclear events. The report is a part of a project aimed to produce a design proposal for a measurement and reporting system with the purpose to increase the Swedish national capability to detect, warn, and inform about nuclear events, with focus on nuclear explosions on Swedish territory and nearby areas. The system should also have the capability to detect other nuclear events, such as nuclear tests conducted at larger distances from Sweden, or smaller releases from nuclear facilities. The project is financed by the Swedish Civil Contingencies Agency (MSB) and the Swedish Ministry of Defence.

In a first report [1] (in Swedish), initial high-level specifications were formulated in cooperation with potential users of information from such a system. The system should be able to report the occurrence of nuclear events as quickly as possible to relevant parties. The system should report the time of the event, geographic position, and, in the case of a nuclear explosion, estimates of height and yield in order to be able to make predictions of direct effects as well as radioactive fallout. A first report should be produced within a short timeframe, followed by updates at regular intervals. The system should have a well optimized alarm threshold in order to avoid false alarms. A reactor accident or a large chemical explosion should for example not be reported as a nuclear explosion.

Reliable information of this kind is best produced using a stationary measurement network as a base, with the possibility to incorporate information from, *e.g.*, mobile sensors which formally may not belong to the system. Here, we assume that the stationary measurement system can include sensors for seismic and infrasound signals, as well as different kind of sensors for radioactivity measurements, such as aerosol filter stations equipped with high-resolution (HPGe) gamma detectors, other spectroscopic gamma systems (NaI detectors), gamma dose rate instruments, or systems for analysis of atmospheric radioactive xenon.

In order to investigate the measurement capability of different sensor- and network configurations, computer simulations was performed. A software framework was created, which can simulate the network response from fictive source scenarios, such as nuclear explosions, or a nuclear release without an associated explosion. The system simulates the response caused by waveform signatures (seismic and infrasound) from explosions conducted underground, in water or in the atmosphere, as well as releases of radioactive aerosols and noble gases. For the waveform technologies, detection and location capabilities were estimated using empirical models, and for the radioactivity sensors, measurements of gamma dose rates, isotopic specific activities, and activity concentrations were calculated in more detail, using atmospheric transport calculations of both particles and gases. For the spectroscopic gamma measurements, synthetic spectra were also produced for each simulated scenario. Localization using radioactivity sensors together with backward atmospheric transport modelling was not simulated, but is planned to be included in later versions.

Although the software framework can be used to simulate a variety of nuclear event types, occurring anywhere on earth, this study focusses on nuclear explosions in Sweden and in nearby areas. The software system is designed to

allow analysis of different systems designs by exposing the systems to large sets of synthetic nuclear explosions, geographically evenly distributed in selected areas. The individual measurement results can then be used to construct at set of key network parameters for each measurement technology which are assembled into a meta dataset that in turn was used to calculate a set of high-level network figures of merit (FOMs), as well as other parameters. The FOMs are intended to facilitate a comparison of the performance of different network geometries and sensor combinations with respect to for example detection and location capability.

The goal of the simulations is not to reproduce individual results for all included measurement technologies, as the modeling sophistication varies; while the response of the aerosol collection systems and NaI detectors are modeled in detail, the waveform simulations contain a higher degree of simplification. Instead, the intention has rather been to make models sufficiently comprehensive to offer a holistic overview of a sensor network performance, and to use such results in selecting between different network configurations.

In addition to simulate network performance, the developed framework can be used for other purposes. The synthetic gamma spectra could for example be used in nuclear emergency exercises, where a release from a nuclear power plant accident is considered, or when evaluating measurement conducted using existing measurement systems.

The framework was also used to produce web-browser based interactive maps of the different calculated explosion and release scenarios. These maps can be used as tools for example when planing and conducting exercises, and in more general discussions on nuclear explosion effects.

The report is organized as follows: The general design and functionality of the modelling tool is given in section 2, followed by a description of the modelling of the nuclear source vector in section 3. The dispersion calculations used to model the particle and gas transport in the atmosphere from source to sensor are described in section 4. Section 5 discuss decay calculations along with the modelling of the different sensors for sampling and measurement of radioactivity, followed by the simulations of seismic and infrasound networks in section 6 and 7, respectively. In section 8 results from a fictitious network are show to illustrate software functionality. The interactive maps are described in section 9, and finally conclusions and outlook are given in section 10.

2 General methodology

This section covers a high-level description of the software framework developed to simulate how a sensor network will respond to nuclear events. The software is named NEMOS (Nuclear Event Monitoring Simulator). The main purpose of NEMOS is to be able to answer how well a particular sensor configuration will be able to timely *detect, identify*, and *locate* nuclear events, and in particular, how well the network will perform this task in the case one or several nuclear explosions occurred.

This means that the simulations should be able to answer a number of key questions, which relates to design requirements. These questions are:

- Does the network detect nuclear events with high enough probability?
- If it does, after how long time will it be able to report the event?
- Which sensors in the network detect the event?
- Can the network differentiate between a nuclear explosion and other events?
- How well can the network estimate the location of the event?
- How well can it determine the height and yield of a nuclear explosion?
- How does the verification capability change as a function of distance to the explosion?
- What network configuration is the most cost effective?

	Type of measurement	*Sensitivity*	*Typical reporting time following event*
Radionuclide sensors			
GM tubes	Dose rate	Low	t_{at}+∼10min
NaI detectors (air)	Spectroscopic	Medium	t_{at}+∼1h
NaI detectors (ground)	Spectroscopic	Medium	t_{at}+∼1h
NaI detector (filter)	Spectroscopic	Medium	t_{at}+∼1h
SAUNA III	Radioxenon	High	t_{at}+∼12h
SAUNA Q_B	Radioxenon	High	t_{at}+∼24h
Filtet station with HPGe detector	Aerosols, spectroscopic	High	t_{at}+∼72h
Wave-form sensors			
Seismic sensor network	Seismic waves	High	∼1min
Infrasound sensor network	Difference in air pressure	High	∼1-5h

Table 1: Overview of the types of sensors that are simulated by the release response framework. Typical reporting time is an estimate of how long after an explosion an instrument reports a detection. Radionuclide sensors are often much slower than wave-form sensors to make a detection, as radioactive material must be transported from the event to the sensor position for a time t_{at} before a measurement is even possible. For a typical wind speed of 10 m/s this would mean about 3 hours for a distance of 100 km. Each radionuclide sensor also have different measurement times due to differences in sample collection, preparation, and measurement integration time.

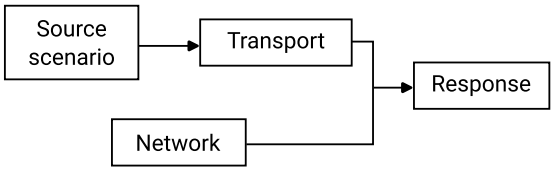

Figure 1: An high-level view of the code architecture for simulation of one scenario.

NEMOS takes information about an explosion or other nuclear event, with the needed input data, and combines this with a sensor network configuration, and simulates the system response. The source code is Python-based and designed to be modular, so that combinations of different source terms, network configurations and explosion sites and times can be investigated (see figure 1).

We will assume a network containing sensors for seismic and infrasound detection, as well as different types of radioactivity measurement systems (overview in Table 1, more detail in sections 5, 6, and 7). Each sensor type will require different input data for realistic modelling. Radionuclide sensors requires a nuclear source term, *i.e.*, a vector containg the amount and types of produced nuclides, release position and time, as well as as an atmospheric transport model (ATM) predicting how the radioactive material is transported from the release to the sensors by the weather. From ATM the amount of radioactive material reaching a sensor as a function of time can be deduced, and the response for that specific sensor can be modelled. The modelling of the waveform sensors, which measure explosion signatures, require information on the power of the explosion (nuclear yield in the case of a nuclear explosion), time and location (including height or depth), environment (for example if an explosion is conducted above water or land), and a model how the explosion energy is transformed into sensor readings of seismic amplitudes or pressure differences in the atmosphere. In addition, the location capability of different waveform networks is possible to estimate. In the current version of the program, we do not model the location capability using radionuclide measurement systems.

The framework also allows simulation of network responses to multiple source scenarios that can be analyzed together. For this purpose, a set of figures of merit (FOMs) were designed to assess the performance of a sensor network to a set of nuclear events, considering factors such as detection capability and minimum reporting time (see section 2.4). By simulating the response to the same set of events for two separate networks, and calculate the FOM for each network, they can be compared and contrasted. It is further possible to optimize a network of sensors by considering what additions of sensors will improve the FOM the most, taking for example cost into account.

The work-flow for when evaluating *one* sensor network and *one* source scenario is described in section 2.1. The work-flow when *set of source scenarios* are evaluated for *one* network is described in section 2.2.

2.1 Network response for one source scenario

The highest level of the code architecture is shown in figure 1. The input contains source scenario details and network configuration, and the output is the response of the sensor in the network to the release scenario.

2.1.1 Source scenario

The first step is to choose a source scenario, defined by the following properties:

- **Nuclide vector** - The nuclides created at time=0 for the event. The case nuclear explosion is discussed in section 3.
- **Explosion yield** - If the scenario is a nuclear explosion, weapon type and explosion yield is defined.
- **Position and height** - The position (lat, lon) and height or depth of burial at which the event occurs.
- **Environment** - If the explosion is conducted above or in water or on land, which has consequences for the signal transport.

2.1.2 Transport

This is a pre-process step, where the transport of both the radioactive material and waveform signals are simulated. Due to the different chemical properties of noble gases compared to aerosols, these are simulated separately. The transport simulations include:

- **Aerosol transport** - Atmospheric dispersion calculations of aerosols using weather data in combination with a dispersion code. The spatial-temporal distribution of air concentration and ground deposition are calculated (see section 4). Rainout is included in the model.
- **Noble gas transport** - Atmospheric dispersion calculations of noble gases using weather data in combination with a dispersion code. The spatial-temporal distribution of the air concentration is calculated (see section 4).
- **Seismic transport** - Transport time and station amplitudes for seismic P-waves are modelled (see section 6).
- **Infrasound transport** - Transport times and amplitudes for infrasound waves are modelled, taking wind data into account (see section 7). In addition, local winds at the station are used to model the noise at the station.

Nuclear decay is not included in the atmospheric dispersion step. It is instead performed in a post-processing step (see section 5.1), when calculating of the response of the radioactivity sensors.

2.1.3 Network of sensors

A network of sensors is defined by:

- **Type of sensors** - It is possible to include a wide variety of different sensors in the network (seen in Table 1), that can detect either radioactive material from a nuclear event, or in the case of an explosion, a waveform amplitude. Sensors are treated differently depending on type, but noise levels and sensitivity is always modelled.
- **Position** - The position of each sensor in the network.

	Aerosol transport ground deposition	*Aerosol transport air concentration*	*Gas transport air concentration*	*Seismic amplitude*	*Infrasound amplitude*
GM tubes	X	X			
NaI detectors (air)		X			
NaI detectors (ground)	X				
NaI detector in aerosol system		X			
SAUNA III			X		
SAUNA Q_B			X		
HPGe detector		X			
Seismic network				X	
Infrasound network					X

Table 2: Transport processes used when calculating detector response.

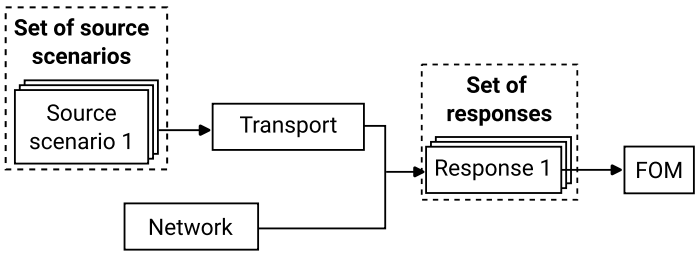

Figure 2: Code architecture used when investigating a set of scenarios. The results can be used to calculate figure of merits for the selected combination of network configuration and scenario set.

2.1.4 Response calculations and results

The response from each sensor is simulated by combining the transport simulations with the network details. Which sensor that uses which transport simulation is shown in Table 2. Some derived properties are universal for all sensors, such as if the signal from the event is detected or not, and the time elapsed from the event to the detection. There are also sensor-specific properties, such as which nuclides that are found using a HPGe or a SAUNA radioxenon detector, waveform amplitudes in infrasound or seismic sensors.

From the response of each sensor, properties of the whole network can be deduced, such as if the event is detected by any sensor, if and how well the event is located, and how long it takes for the event to be detected. These quantities can be used to evaluate the network, and to understand the response to different types of events.

2.2 Response of a network for source scenario sets

To statistically investigate the response of a specific configuration, the sensor network is evaluated with respect to a set of source scenarios. The process for this is very similar to the one outlined in section 2.2, however, with the response of the network being calculated for multiple source scenarios instead of just one (see figure 2). In addition to the sensor-specific network responses to each event, aggregated attributes are calculated, such as what percentages of the events are detected by the network. The aggregated attributes are used to find the figure of merit (FOM) for the combination of a network of sensors and a source scenario set. This can then be used in several different types of evaluations and comparisons. We can evaluate the FOM for one network to several different source scenario sets, *e.g.*, how does the FOM change if we assume events randomly scattered across Sweden compared to events randomly

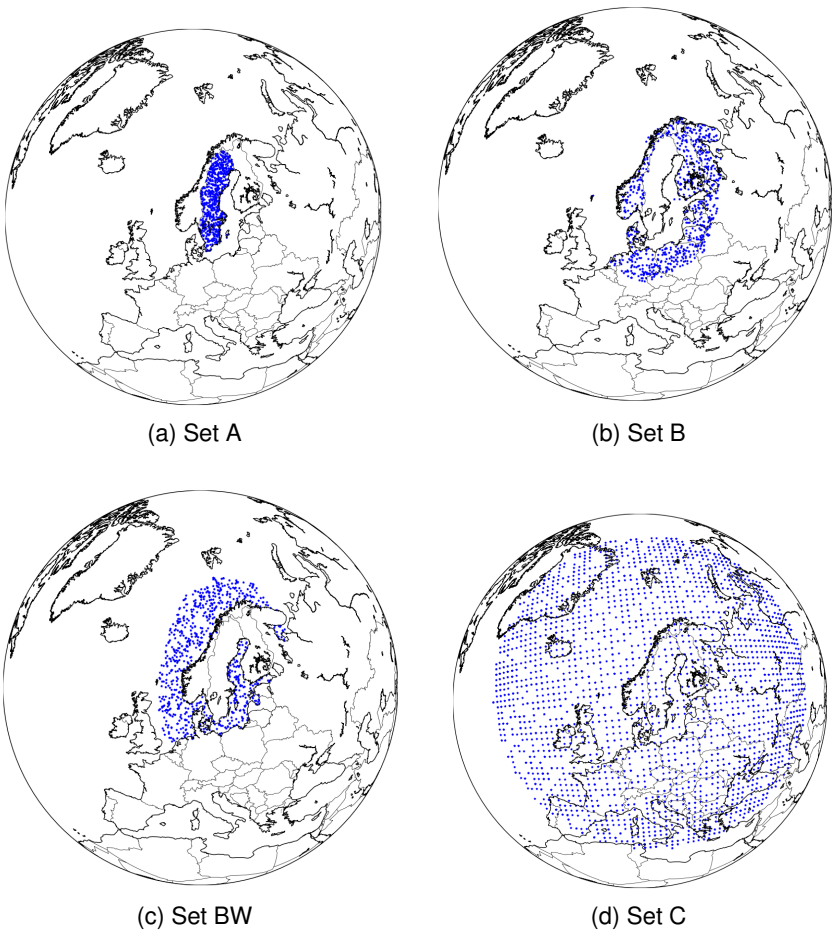

(a) Set A (b) Set B

(c) Set BW (d) Set C

Figure 3: Overview of the different case scenario sets.

scattered across Europe. It is also possible to use the same source scenario sets to evaluate two different network configurations, to determine which provides most utility. It is further possible to investigate what additions of sensors will improve the FOM of a current network, e.g. investigate how doubling the number of GM sensors changes the FOM. This approach can be used to optimize the performance of a network, with regard to, *e.g.*, cost of the sensors, or speed of detection.

2.3 Source scenarios

Several source scenario sets were created, differing with respect to spatial distribution relative to Swedish territory.

- **Set A** - Explosion on Swedish territory. Two random start times and coordinates per day during a year, resulting in 730 events.

- **Set B** - Explosion in a land area covering a distance up to 700 km from Sweden, excluding Sweden itself. Two random start times and coordinates per day during a year, resulting in 730 events.

- **Set BW** - Explosion in areas covered by water at a maximum distance of 700 km from Sweden, excluding Sweden. Two random start times and coordinates per day during a year, resulting in 730 events.

- **Set C** - Explosions in Europe. Ten random start times per day during a year, at coordinates randomly chosen from a rectangular grid, resulting in 3650 events.

The sets are shown in figure 3.

2.4 Figures of Merit definitions

Before we define the FOMs, we need to define the measurement system and its responses. A measurement system M is defined by a collection of sensors networks of different types (for all sensor types, *reporting time* is defined as the time difference between the true event time and the time when a detection is observed):

- A **seismic network** S consisting of N sensors: $\{S_1, S_2, .., S_N\}$. The seismic network response E_S is an event defined by a detection flag (detected/not detected), event time, reporting time, body-wave magnitude m_b, coordinates (lat, lon) and an error ellipse (σ_x, σ_y). The depth of the event is set to zero. Detection requires at least four detecting sensors with an amplitude $A > 3 \times snr$, where snr is the signal-to-noise ratio. A sensor can be either a single seismometer or a seismic array.

- An **infrasound network** I consisting of M sensors: $\{I_1, I_2, .., I_M\}$. The infrasound network response E_I is an event defined by a detection flag (detected/not detected), event time, reporting time, pressure P, coordinates (lat, lon) and an error ellipse (σ_x, σ_y) or polygon area. Detection requires at least two detecting sensors. A sensor consists of 3 elements.

- A **radionuclide network** R consisting of K sensors: $R_1, R_2, .., R_K$. The radionuclide network response is defined by a set of measurements $E_R = \{C_1, C_2, .., C_P\}$ where each C_i consists of detection flag (detected/not detected), reporting time, and one or more of the observables dose rate D, activity A and activity concentration AC. The observables A and AC are nuclide specific. Detection is defined as $D > 2 \times$ average background or A $(AC) > MDA$ (MDC), and requires at least one detecting measurement from at least one sensor. If A or AC is detected for a nuclide, a nuclide is considered *identified*. In the case only dose rate is measured, nuclide identification is not possible.

A given measurement system configuration $M = \{S, I, R\}$ will produce a set of system responses $E = \{E_1, E_2, .., E_N\}$ from a set of N nuclear explosions $i = 1, 2, .., N$, where $E_i = \{E_S, E_I, E_R\}$.

Five figure of merits (FoMs) are calculated from the set of resonses E, all defined as fractions of a set of nuclear events where different conditions are fulfilled:

- **Detection Power (DP):** The fraction of events for which E_i results in at least one detection in S,I, or R.

- **Location Power (LP):** The fraction of events for which E_i results in a location error less than x km for a seismic detection, and less than y km for an infrasound detection. x and y are case dependent.

- **Reporting Power (RP):** The fraction of events for which E_i results in at reporting time less than t_r (case dependent).
- **Nuclear Explosion Identification Power (NEIP):** The fraction of nuclear explosions for which E_i results in an identified nuclear explosion. A nuclear explosion is identified when
  - A detection from S or I and at least two CTBT-relevant nuclides (see below) are identified, or alternatively,
  - A detection from S or I and R.

  NEIP is defined only if the scenario nuclear explosion is investigated. The first alternative implies a more strict requirement than the second.
- **Nuclide Identification Power (NIP):** The fraction of events for which E_i results in at least one identified nuclide. This FOM is mainly intended for other nuclear event scenarios than nuclear explosions.

The CTBT-relevant nuclides list is used in verification of the Comprehensive Nuclear-Test-Ban Treaty [2]. It is possible that other, more short-lived, nuclides than the ones included in the CTBT-list could be used to detect a nuclear explosion, and potentially increase FOMs like NEIP and NIP. Location and reporting power both rely on an analysis of a distribution (uncertainty area and reporting time, respectively). Obviously a more elaborate statistical analysis of such distributions is possible than using a simple cut-off, such as calculating the mean, minimum, maximum, and width of the distributions. Also, it should be mentioned that FOMs also can be calculated for individual subnetworks, in order to gain more detailed information (for example *nuclear reporting power* or *infrasound detection power*). Another option is to require the conditions for the FOM to be fulfilled within a certain time after the explosion (see section 8.5, where the FOM:s NEIP24 and NIP24 requires their respective FOM conditions to be fulfilled within 24 hours).

3 The nuclear source term

3.1 Introduction

NEMOS can in principle be used to model the response from any nuclear event scenario, defined by release time, duration, position, and initial nuclide distribution (or *nuclide vector*). In this report, we focus on nuclear explosion scenarios, and in this section, the modelling of nuclide vectors for this case is described in general terms. A more detailed description will be published at a later date [3].

3.2 Modelling the nuclide vector

The first step in the process of estimating the fallout from a nuclear explosion is to define the nuclide vector, *i.e.*, the set of nuclides that through several processes is produced in the detonation. The nuclide vector can be estimated using progressively advanced methods for a more realistic result. Key aspects are the level of sophistication in the modelling and the type of nuclear processes included. A common, simple starting point is to only include the fission products produced based on tabulated values of independent fission yields for a single neutron energy, representative of the typical neutron spectrum in a detonating nuclear weapon, and the number of fissions. Improving on this approach, tabulated values for a number of neutron energies, weighted by the typical fission spectrum, can be used. Any more advanced model presupposes a more detailed knowledge of the inventory of fissile nuclides, fusion fuel and the neutron spectrum as they evolve over time during the detonation. The model presented below, implemented in a computer program, aims to achieve a realistic description of the nuclear processes and the transport of neutrons in the device, with some simplifications mainly in the treatment of neutron transport.

Another important modelling aspect is the hydrodynamic behaviour associated with the detonation, which can affect the nuclear processes, mainly through the varying density in the fuel during the detonation and through the temperature variations in the fusion fuel, in case the device contains a second stage. No dynamics is included in this model. The densities has been set to reasonable values fixed over both time and space in the different parts of the device.

A final piece of the modelling task is the description of the transmutation of non-nuclear material, due to the nuclear blast. This includes construction materials and electrical parts of the weapon, and, if the burst is close to ground or water, the elements in the ground or water below the detonation. The parameters listed above are more or less unknown, but educated guesses can be made and the effect of varying the different parameters can be calculated. The program can be used to calculate the nuclide vector for a number of representative cases or for a larger parameter space. In this work, three representative cases were modelled (see section 3.3).

3.2.1 Materials produced in nuclear explosions

A nuclear explosion is an extremely energetic event involving high temperatures and a huge number of nuclear particles reacting in different ways, transforming nuclei from one type to another. Both fission and fusion release a large number of energetic neutrons which can interact with other nuclei, either in the fuel

or in the surrounding materials. These interactions can lead to more fission or transmutation, creating new isotopes. Additionally, other nuclear processes take place in the fuel on a much longer time scale compared to the nuclear explosion. Such processes have been disregarded in this work.

As noted above, neutrons leaking from the fuel can interact with surrounding materials. For the majority of nuclides four different nuclear reactions dominate: a reaction where no secondary particles are released (except for a photon), reactions where a proton is emitted, reactions where an alpha particle is emitted, or reactions where two neutrons are emitted. The rate of the different processes depends on the likelihood for each respective process, which, in turn, depends on the energy dependent cross section. This is true for non-nuclear material in the weapon, in the air and in the ground. The nuclide vector computer program can calculate the rate of the different processes using pre-calculated nuclear data, as discussed in the following four subsections.

3.2.2 Fission products

Nuclear fission is a reaction in the atomic nucleus, where the original atoms split into two (or more; not modelled here) daughter nuclides after colliding with a neutron, simultaneously releasing a large amount of energy. In addition to the two new nuclei that are formed, a number of neutrons are released. The fission products are often rich in neutrons compared to the number of protons and they are often, for this and other reasons, unstable and decay to other nuclides. The fission products are the main source of the short lived activity (in this context meaning a half-life of less than 100 years).

Even though the outcome of an individual fission event is random, on average two to four neutrons are released depending on the energy of the absorbed neutron. The average is called $\bar{\nu}$ (or "nubar") and has a value slightly above two for the most common fissile materials at lower neutron energies.

The most common isotopes in fission fuels are ^{235}U and ^{239}Pu, but uranium always contains a small admixture of ^{238}U and plutonium ^{240}Pu. Due to the transmutation of the fuel during the explosion, smaller amounts of even heavier isotopes will also be present at the later stages of the explosion. Therefore the data files used by the program contain the probability of a certain nuclide being produced as a fission product for a number of uranium and plutonium isotopes for a large number of neutron energy groups spanning from 0.1 MeV to 14 MeV, as well as nubar for the same set of isotopes and energies. The data also includes the probability for the creation of excited states of the fission products, so called isomers.

The data for the fission products have been calculated and tabulated using the computer program GEF[4]. As the nuclear process is random, GEF uses a statistical method implementing a detailed physical model with randomized elements. The result will therefore depend on the number of samples. The data used here is based on a large number of samples giving results converging to the maximal internal precision available in GEF. The neutron multiplication factor nubar comes from the neutron library ENDF-VIII.0 [5] after being evaluated and adopted from the semi-continuous data in the library to a discrete group structure, using the computer program NJOY21 [6].

3.2.3 Neutron activation products

During a nuclear explosion, the surroundings becomes flooded with neutrons, and some of the nuclei in the surroundings absorb neutrons that have leaked out of the fuel. Typically, the resulting nuclei are radioactively unstable. Such

neutron activation occurs in the non-nuclear materials in the weapon, and if the explosion occurs close to the ground, in the ground material. Therefore, the resulting neutron activation products, depend on assumptions of the weapon material and on the ground composition.

3.2.3.1 Neutron activation in weapon materials

An exact value, within the approximations made, for the number of neutrons leaking out of the fuel is calculated by the program; but as a rule of thumb 0.5 neutrons per reaction, fission or fusion, will reach the surrounding non-nuclear materials in the weapon. The exact composition of the non-nuclear materials is of course a well kept secret, but there will most probably be alloyed steel, aluminium and titanium there as well as high explosives and cables and other electrical components. Each nuclide present in the weapon has some probability to absorb a neutron based on the neutron energy. To decrease the size of the large datasets needed, the input data is averaged over the typical neutron energies of interest. The averaging procedure has been performed using MCNP [7], where simplified generic models of a primary and a secondary have been used to transport neutrons produced by fission and fusion respectively, using a detailed physical model including moderation, slowing down of the neutrons due to elastic collisions with nuclei in the weapon, and other nuclear processes. The reaction rate for four different absorption processes have then been calculated for all nuclei available in the library from hydrogen to thorium.

The result has been tallied as grams produced for each individual reaction for each neutron and gram of the nuclide present in the initial configuration. Secondary effects were one nucleus already transformed absorbs another neutron are not included. The total production of a specific nuclide is calculated as the sum of the production from all the processes on different nuclei yielding the same final nuclide. If the number of produced nuclei is higher than the number of neutrons leaking out from the fuel, indicating that all the neutrons are absorbed in the non-nuclear part of the weapon, the production is evenly scaled with the actual number of neutrons.

The actual geometric distribution of materials in the weapon has not been modelled, since this information is not available. The neutron flux is assumed to be isotropic, the same in all directions, and the material evenly distributed around the neutron source.

3.2.3.2 Ground and air activation products

The neutrons not absorbed in the weapon can react with nuclei in the air and, if the explosion is close enough, in ground material. The mean free path of fast neutrons in air is approximately 150 m, and beyond two mean free paths the neutron flux is too low to be of any importance. The exact cut-off is somewhat arbitrary, but the optimal height of burst for all but the smallest weapons are higher. The typical scenario would either be a ground burst (for destroying hardened targets) or an air burst much higher than 300 m making the exact details less important.

For an air burst the neutrons are first travelling through air, transmutating the nuclei in the same way as for the non-nuclear materials in the weapon (with one difference, see below). If the distance to the ground is less than 300 m the fraction of the neutrons reaching ground (the rest being absorbed by air) will transmute nuclei in the ground material.

The data for this part of the calculation is produced in a similar way as the data for the weapon materials, described in the section above, but with more moderation as the neutrons, on average, have passed through more air

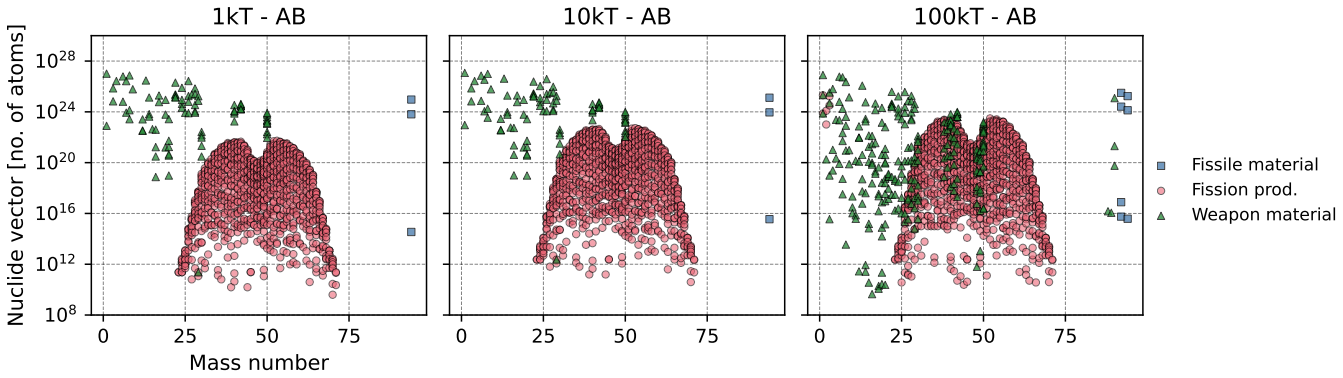

Figure 4: Produced nuclei for three atmospheric nuclear explosions with different yields.

and ground before reacting with a nucleus. Another difference compared to the weapon materials are that while there is a finite number of nuclei in the weapon compared to the number of neutrons the number of nuclei in the air and ground is effectively infinite compared to the number of neutrons so we know that all neutrons will sooner or later be absorbed. The number of nuclei undergoing a nuclear reaction in the weapon depends both on the absolute rate of each reaction, the number of neutrons, and the number of nuclei of each type being available in the initial configuration. The number of nuclei in the air and ground instead only depends on the number of neutrons and the relative rates of the reactions.

3.3 Explosion scenarios

Three explosion yields were calculated with the nuclide vector code, to represent different type of scenarios:

1. **1kt** - a low-yield scenario, fission weapon with plutonium (^{239}Pu) as the fissile material.
2. **10kt** - a intermediate-yield scenario, fission weapon which, similar to 1kt, assumes plutonium (^{239}Pu) as the fissile material, however, with a higher yield.
3. **100kt** - a high-yield scenario, multi-stage thermonuclear weapon, with 50% of its yield from fusion. The primary contains both uranium (^{235}U, ^{238}U) and plutonium (^{239}Pu) as fissile material.

For now we only consider *air bursts (AB)*, when the explosion happens at some optimal height to maximize the damages from the shock wave, however, it should be noted that *ground bursts (GB)*, when the explosion happens at ground or sea level, is possible to model as well.

In figure 4, the resulting products are shown for the three airburst explosion scenarios. While there are differences in how much material forms for different types of weapons and yields, depending on assumptions of the non-nuclear weapon material, the overall trend is similar; a majority of the produced nuclides are due to fission, showing up as a double peak distribution. Neutron capture of weapon material results mostly in low-to-intermediate mass nuclides, while neutron capture in the fissile material produces actinides and transuranium nuclides. In the following text we use the shorthand *yield-burst type* for each scenario (e.g. *1kt-AB* for the 1kt air burst scenario).

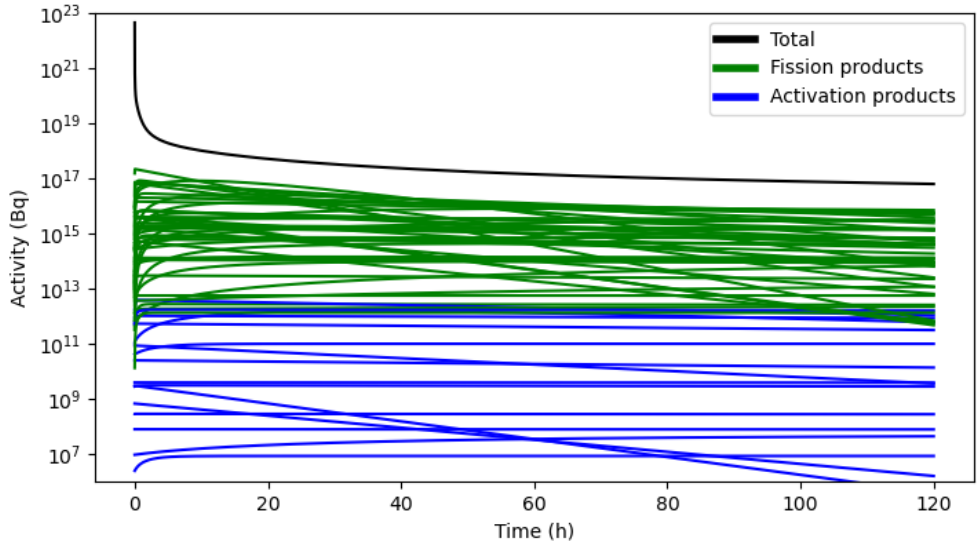

Figure 5: The time dependence of the activities of the CTBT-relevant nuclides following a 1 kt explosion conducted using a ^{239}Pu fission device at a height maximizing the shock wave (scenario 1 in section 3.3. The total activity includes all nuclides produced.

To illustrate the difference between fission and activation, the time dependence of the activities of the CTBT - relevant nuclides produced in the 1 kt explosion is shown in figure 5. As the figure illustrates, activation products contribute to a much smaller extent to the total activity.

3.4 Comparing the result with other nuclide vectors

The yields from our nuclide vector model is compared to two other nuclide vectors; *1kt-AB* is compared to results from a 1 kt pure ^{239}Pu explosion based on data from the ENDF/B-VIII.0 [5], and *100kt-AB* is compared to yields from a 100 kt fusion bomb presented in a report by the Swedish Radiation Safety Authority (Strålsäkerhetsmyndigheten, SSM) [8].

3.4.1 Comparison with ENDF

The ENDF/B-VIII.0 [5] library provides the fission yields from a reaction with neutrons of constant energy of 0.5 MeV with either ^{235}U or ^{239}Pu, or for fast neutron of constant energy 14 MeV with ^{238}U. Given fissile material and explosion yield, the fission product yield can be calculated from this data, which is done for a 1kt ^{239}Pu explosion and denoted as *1kt-ENDF* in the following text. This is compared to the *1kt-AB* case, calculated with our nuclide vector code, described in Sect. 3.3.

Figure 6 shows the population against mass number for yields for *1kt-ENDF* and for the *1kt-AB* case. As seen there are several nuclides missing from the ENDF results as no neutron activation products are included. The shape of the double-peak distribution is very similar for both cases, with some key differences; the wings are slightly wider, and the dip at mass number 120 is slightly shallower for the *1kt-AB* case.

Figure 7 show a comparison per nuclide, for nuclides with population over 10^{19} that are present in both the ENDF results and in *1kt-AB*. The yields for

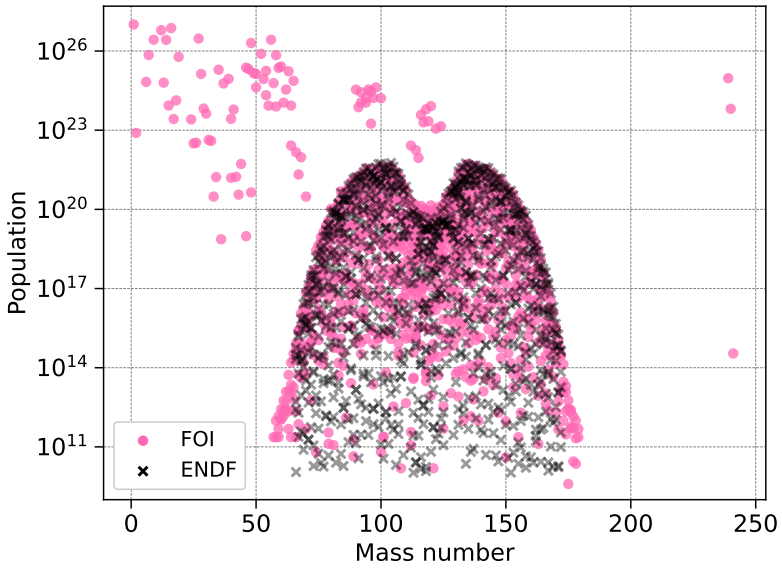

Figure 6: Comparison with ENDF data for 1kt explosion with fissile material ^{239}Pu.

both cases are overall similar. The shallower dip in the double peak distribution for our nuclide vector can be observed around mass number 120. A handful of nuclides, ^{94}Zr, ^{96}Zr, ^{100}Mo, ^{122M}In and ^{124}Sn, are more abundant in the *1kt-AB* case, as they are formed by both fission and neutron activation.

The yield differences are a consequence of our nuclide vector model being more sophisticated, including a more realistic neutron energy distribution, and the inclusion of neutron activation processes.

3.4.2 Comparison with SSM nuclide vector

A nuclide vector of a 100kt fusion bomb was presented in a report by SSM (for details, see [8], Appendix 3), denoted as *100kt-SSM* from now on, which provides us with an opportunity to compare with a more higher-yield nuclide vector, where different fissile material and neutron activation are taken into account. It should also be noted that *100kt-SSM* was developed for dose calculations, not for detection purposes, and therefore model design choices always used the alternative that minimized the risk to underestimate the dose.

100kt-SSM is semi-empirical nuclide vector, and has two main components: fission products from the fissile material, and activation products from the weapon material and the surroundings. The fission products are approximated using the method presented in [9], which uses ENDF data scaled according to the fissile material used in the weapon. Three fissile materials are considered: the fission of ^{235}U and ^{239}Pu by 1 MeV neutrons assumed to occur in the primary, and the fission of ^{238}U by higher-energy 14 MeV neutrons induced by the fusion reaction in the secondary.

The second component is activation products from both the weapon material and from the surroundings. These are based on KDFOC3 [10], a nuclear fallout code (see also section 4), and a analysis of activation products from nuclear tests at the Nevada test site (discussed in Sect. 3.2 in Appendix 2 of [8]).

After adding the two components of the nuclide vector, a selection of nuclides relevant for the dosage are made (Sect. 4 in Appendix 2 of [8]). *100kt-SSM* is the nuclide vector of the main scenario, 100 kt ground burst with 50%

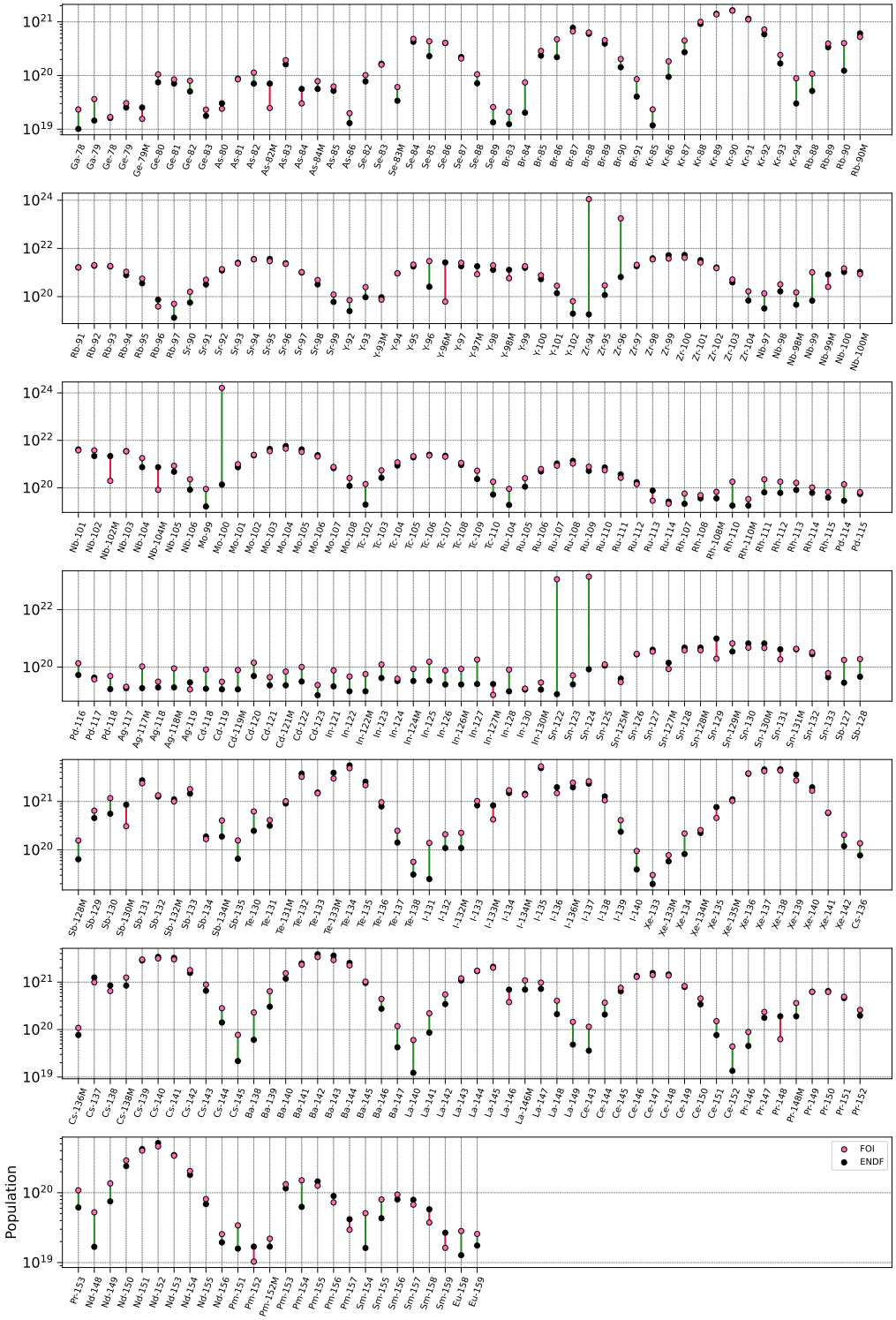

Figure 7: Comparison with ENDF results, per nuclide with population over 10^{19} that are present in both.

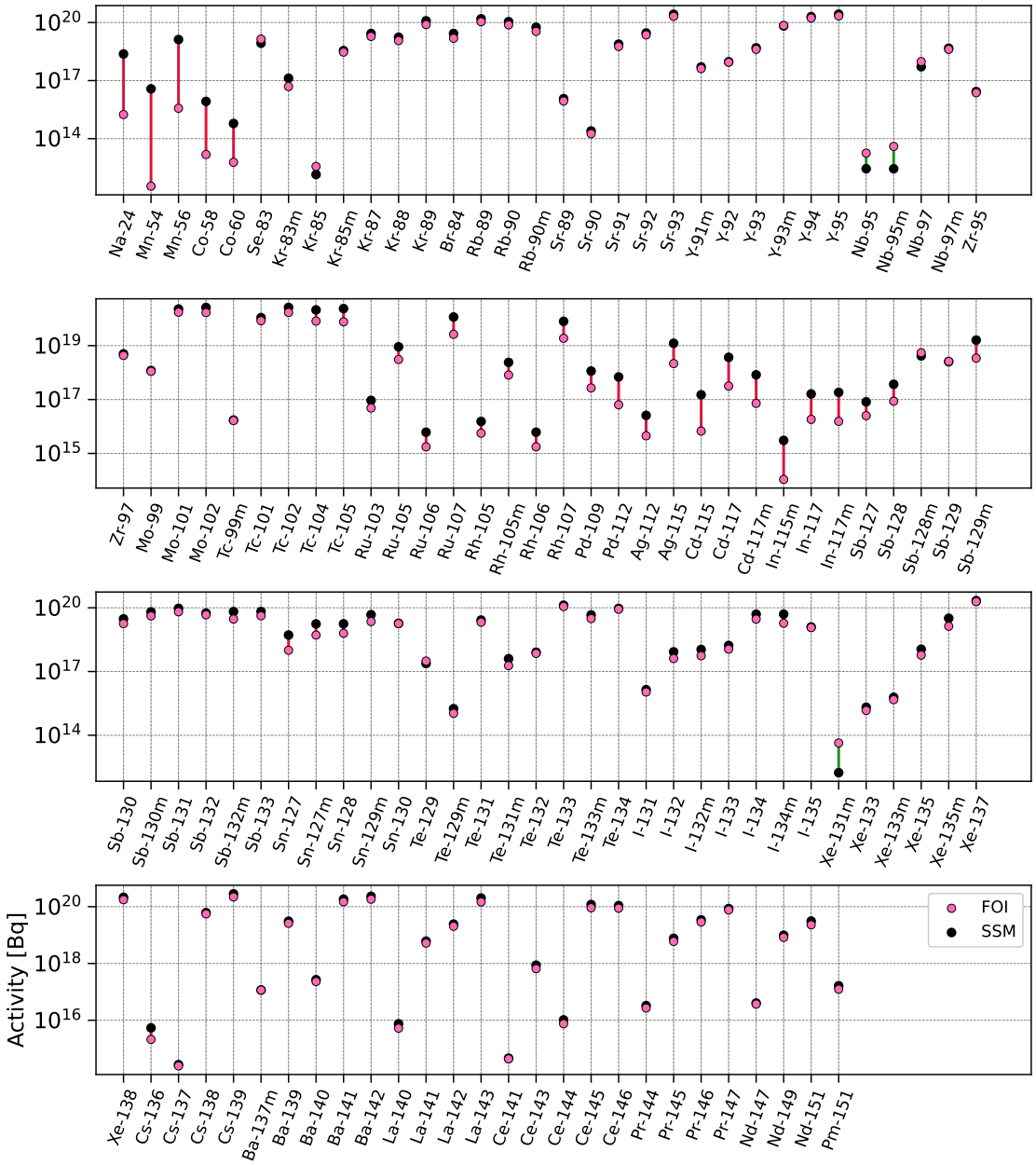

Figure 8: Comparison between *100kt-SSM* from the SSM report [8], and the in-house model *100kt-AB*, for all overlapping nuclides. As in the SSM report, the nuclides are presented as activity 10 minutes after the explosion.

fusion, is shown in table 2 in [8]. They present their nuclide vector, which has been reduced to include isotopes of special interest, in activities 10 minutes after the explosion. *100kt-SSM* is compared to the *100kt-AB* scenario. Using the decay equation 5.6 and equation 5.9 described in section 5.1, the activity at 10 minutes can be found for *100kt-AB*, and a comparison of the isotopes present in both is shown in figure 8. Note that three isotopes that are present in *100kt-SSM* are not present in *100kt-AB*; ^{7}Be, ^{58m}Co, and ^{203}Pb. According to [8], these are from weapon material, and thus depend on the assumption about the weapon.

As *100kt-AB* is an airburst explosion, while *100kt-SSM* is a ground explosion, the later will include neutron activation of ground material which is absent in our modeling. This explains the large differences in abundance of ^{24}Na and ^{58}Mn, which is from ground material in the SSM model. Similarily the differences in ^{54}Mn, ^{58}Co and ^{60}Co are due to assumptions about the weapon materials used.

Overall, however, the trends seen in both nuclide vectors are similar except for the mentioned isotopes. There are some increasing differences around mass number 120, which indicate discrepancies in of the dip of the double-peak distribution, likely caused by differences in modeling methods.

4 Atmospheric dispersion calculations

4.1 Introduction

The atmospheric dispersion calculations were conducted using two different dispersion codes: Dispersion Engine (DE), which is a computational framework developed at FOI, was used for aerosol transport, and HYSPLIT [11] was used to model xenon gas. Due to their different chemical properties compared to aerosols, noble gases are simulated separately. Noble gases will for example not be washed out by precipitation. No radioactive decay was modelled in the dispersion calculation step. This was done in a post-processing step using the resulting spatial-temporal distribution of the dilution factors obtained from DE and HYSPLIT (see section 5.1).

4.2 Modelling of particulate dispersion

4.2.1 Source model

Atmospheric dispersion simulations were conducted to estimate the distribution of particulate radioactive material following a nuclear explosion. A nuclear explosion includes many complex physical and chemical processes which have been the targets for comprehensive research ever since the start of the development of nuclear weapons. The heat created in the fireball will instantly transform present material into gas and plasma. For explosions close to the ground, strong updrafts induced by the heated air lifts ground materials high into the atmosphere where it will be part of the residual radioactive material and be subject to atmospheric dispersion. The fate of the radioactive material depends to a high degree on the particle sizes. Large objects, such as rocks, will quickly fall down to the ground while smaller particles are transported further. The smallest particles might be transported over long distances and deposit on the ground due to different removal processes such as dry and wet deposition.

In the 1960's, an empirical model for short range nuclear fallout was developed, based on US nuclear tests in the Nevada desert. The model was named KDFOC and mainly describes how the activity is distributed over particle sizes in the cloud when the initial intense period of the explosion has passed and the cloud has stabilized. KDFOC assumes that the stabilized cloud is obtained approximately five minutes after the explosion. The cloud is modelled to consist of four main sections which are referred to as the *main cloud*, the *stem cloud*, the *ground zero circle*, and the *base surge cloud*. These sections are further divided into finer subsections to improve the spatial description of the radioactive material. Depending on the height and yield of the bomb, some of the sections might be non-existent. The source term depends on the yield of the bomb, the fission fraction, and the release height. Moreover, some ground characteristics are specified to capture the interaction with the ground.

KDFOC is constructed for the prediction of short-range fallout of the radioactive material. It provides predictions of the geometry of the cloud and the activity distribution over particle sizes within each subsection. However, it does not include small-sized particles, i.e. below 5 µm in radius. The small-sized particles are in general transported beyond the area of interest for KDFOC and their contributions to measured activity in the Nevada tests were probably negligible. However, for long-range transport of radioactive material, the small-sized particles are important and therefore a missing key component in KDFOC. To address this issue, FOI has developed a model named Nuclear

Weapon Source With Airborne Model Particles (NWSWAMP) which is based on KDFOC3, i.e. the third model version released in the nineties. The difference between KDFOC3 and NWSWAMP is mainly the addition of small-sized radioactive particles that allows the source term to act as a source term for long-range dispersion models. Moreover, support for applying a nuclide vector and source terms for including the release of inert gases is added in NWSWAMP. A more thorough description of NWSWAMP is presented in [12]. An overview of sections/subsections and their sizes for an 80 kt bomb is presented in figure 9. When NWSWAMP is used as source term for long-range atmospheric dispersion simulations, model particles are introduced in each section separately and according to their assigned activity distributions.

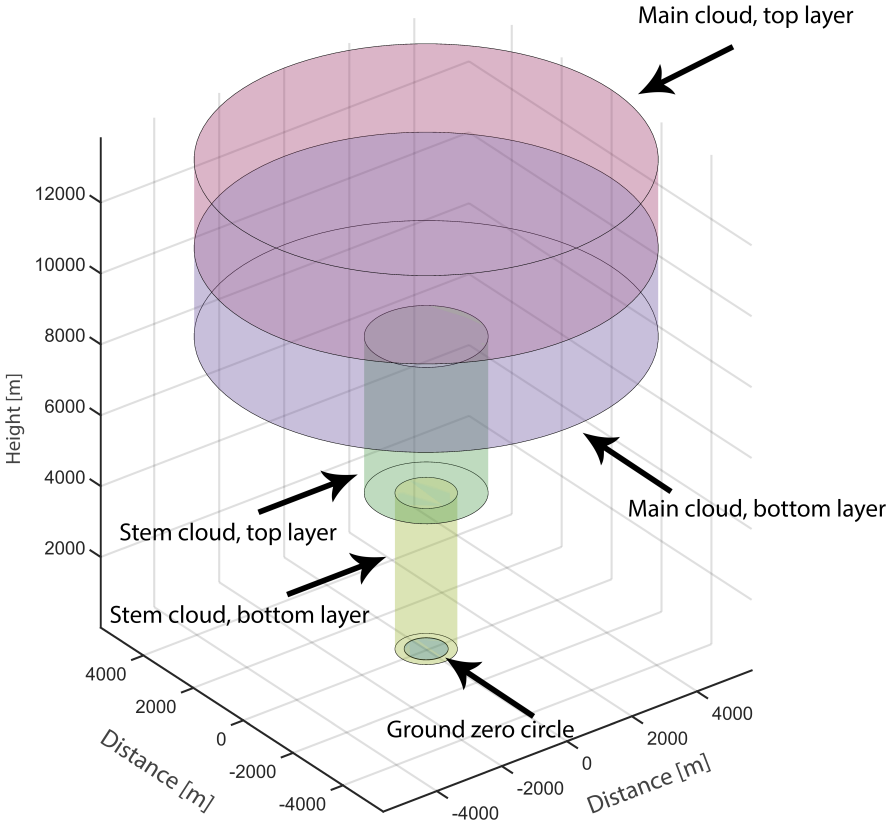

Figure 9: Illustration of the main sections of a mushroom cloud as modelled by NWSWAMP for an 80 kt bomb with 50% fission that explodes on the ground surface. A base surge cloud only appears for underground explosions which is not the case here.

4.2.2 Dispersion modelling and meteorological data

Dispersion calculations were carried out using Dispersion Engine (DE), a modular computational framework for dispersion calculations developed by FOI. Simulations were done in DE using the long-range dispersion model PELLO [13] coupled to the source terms constructed by NWSWAMP. PELLO is a Lagrangian particle model that utilizes random displacement dynamics in the current wind fields. The meteorological parameters used by PELLO, such as wind fields, temperatures and precipitations, are loaded from numerical weather forecasts in GRIB format. For this work the ERA5 catalogue of historic weather from ECMWF (European Centre for Medium-Range Weather Forecasts) was

used. Meteorological data for the entire year of 2018 with one hour time resolution and spatial resolution of 0.25 degrees in both latitudinal and longitudinal directions was used. The geographical region of the simulation were the entire northern hemisphere.

Deposition is an important removal process of radioactive material from the atmosphere to the ground, and it has therefore a central role in the estimation of both airborne and deposited field of radioactivity. The deposition model used in PELLO is described in [14], and includes both wet deposition [15, 16] and dry deposition [17]. The term wet deposition refers to removal by means of precipitation, while dry deposition refers to transport and adsorption to the ground surface by means of other processes.

4.2.3 Simulation protocol

The software required to conduct long-range atmospheric dispersion simulations is comprehensive and involves many physical models and numerical components. However, the process can quite straightforwardly be reduced into a simple scheme on a synoptic level. The estimation of radioactive concentration fields were established by applying:

1. Location, choosing position and time for the explosion
2. Source term, establish a source term by using NWSWAMP
3. Meteorology, loading ERA5-data for the time period of interest
4. Dispersion, applying PELLO to simulate the atmospheric dispersion and deposition
5. Postprocess, calculating the desired concentration fields using information from PELLO

The results from each simulation were two time-dependent concentration fields, one for airborne material and one for deposited material. This scheme was applied to all specified explosion positions and their related points in time, which resulted in an equally large number of simulations.

4.2.4 Source scenario sets

In particular, aerosol dispersion calculations were performed assuming a 1 kt nuclear explosion conducted at a height of 150 m. Simulations were done for the source scenarios A, B, BW, and C, described in section 2.3. To be able to interpret the FOMs related to atmospheric transport,*i.e.*, *Nuclear Explosion Identification Power* and *Nuclide Identification Power* (see section 2.4), the fraction of explosions reaching Sweden was calculated for the four cases discussed in section 2.3. The results are shown in table 3.

As can be seen in the table, a significant fraction of the explosions in case A (Sweden) will not reach the ground level in the model (21% in the case of air, and 13% in the case deposition is modelled). In those cases, all particles will be transported away from Sweden and never reach the ground level. As expected, the fraction reaching Sweden will decrease as the average distance from Sweden decreases for according to the spatial distribution of the explosions in the different case sets.

The distribution of the earliest time the plume reaches Sweden is shown in figure 10. As expected, the distributions for scenario sets in or close to Sweden are more shifted towards shorter times compared to scenario C (Europe).

Case	Type	Total	Within 24 h
A	Air	0.79	0.49
A	Deposition	0.87	0.63
B	Air	0.64	0.17
B	Deposition	0.65	0.18
BW	Air	0.79	0.28
BW	Deposition	0.81	0.33
C	Air	0.58	0.074
C	Deposition	0.59	0.074

Table 3: Fraction of simulated explosion aerosol releases reaching the 0-300 m atmospheric layer in Sweden. The fraction of releases reaching Sweden at any time within 7 days are in the third column. The fraction reaching Sweden within 24 hours are shown in the fourth column.

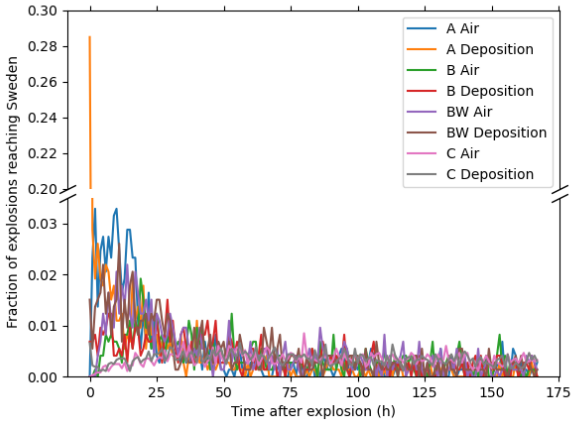

Figure 10: Distributions of the time of first aerosol plume hit in Sweden following a 1 kt nuclear explosion at 150 m. Results are shown for the different scenario sets, separately for air concentration and ground deposition.

4.3 Gas dispersion calculations

Dispersion of the Xenon noble gas from the release coordinates was calculated using the Hybrid Single-Particle Lagrangian Integrated Trajectory model (HYSPLIT), version 5.2.0 [11]. GFS Weather data was downloaded from NOAA's publicly available data server [18].

For each release coordinate and time, 10^6 particles was released for a duration of one hour, assuming a point source at a height of 100 meters, and tracked forward for 7 days. As further discussed in section 8.1, the different height compared to the aerosol model is due to the fact that at present, we don not have access to a proper model for dispersion of noble gases from an atmospheric nuclear explosion, and we used a standard model normally used to simulate underground explosions. The spatial resolution of the weather data input to the calculations was 0.25 degrees. The spatial and temporal resolution of the calculated concentration field was 0.25 degrees and 3 hours, respectively. The concentration field was calculated in a 0 - 100 m layer.

5 Simulations of responses from radiation detectors

5.1 Decay calculations

The nuclide vector described in section 3 provides the starting composition of the fallout from a nuclear explosion. The composition of the fallout will evolve with time, as the original nuclides decays into daughter products. The modelling of this process can be done with the Bateman equation, which describes the abundances of nuclides in a decay chain as a function of time, if the initial composition and the half-lives are known [19]. While it is possible to solve the Bateman equation time-dependence analytically [20], such approach is not suited for large decay chains and can lead to numerical instability as the equations sometime requires divisions with very small numbers. Instead, a numerical approach to find the time-dependent composition is used, where time-evolution of the isotope are described by a system of ordinary differential equations. While there are numerous ready-made code packages that perform such task, a solver was developed to make integration into our simulation framework smoother, and makes it possible to explore more complex decay scenarios.

In this section three different situations dealing with decaying nuclides are described: the time evolution of the nuclide vector, the response of a spectrometer observing particle decay from either surrounding air or ground, and the decay process and response of an instrument where nuclides are collected from air.

5.1.1 General case

The time-dependence of the nuclide vector follows the general decay scenario and is described in this section. The population N of some radioactive isotope i with half-life T_i and decay constant $\lambda_i = \ln(2)/T_i$ will decay with the rate

$$\frac{dN_i}{dt} = -N_i\lambda_i. \tag{5.1}$$

Equation 5.1 has the exact solution

$$N_i(t) = N_i(0)\exp(-\lambda_i t), \tag{5.2}$$

where $N_i(0)$ is the initial number of isotopes i.

If there are other nuclides j that can decay into nuclide i with a branching ratio B_{ij}, an ingrowth occurs such that

$$\frac{dN_i}{dt} = -N_i\lambda_i + \sum_j N_j\lambda_j B_{ji} \tag{5.3}$$

where the left term on the right hand side describes the *destruction rate* $\vec{\mathscr{D}}$, and the right term describe the *production rate* $\vec{\mathscr{P}}$ of species i, so that

$$\mathscr{D}_i = N_i\lambda_i \tag{5.4}$$

and

$$\mathscr{P}_i = \sum_j N_j\lambda_j B_{ji}. \tag{5.5}$$

For a composition with several different isotopes with interconnected decay chains, the time-evolution is govern by the system of ODEs defined by equation 5.6.

$$\frac{d}{dt}\vec{N}(t) = (\vec{\mathscr{P}} - \vec{\mathscr{D}})\vec{N}(t) \tag{5.6}$$

with

$$\mathscr{D}_{ij} = \delta_{ij}\lambda_i \tag{5.7}$$

and

$$\mathscr{P}_{ij} = \lambda_j B_{ji}. \tag{5.8}$$

$\vec{N}(t=0)$ is the starting nuclide vector discussed in Sect. 3. Further, λ_i and B_{ji} are also known using nuclear data from the ENDF/B-VIII.0 library [5].

We can then solve equation 5.6 ODE numerically with the `scipy.integrate.odeint` solver from the Python package `scipy` [21], and find $N_i(t)$ for the nuclides i, where nuclide i is either defined in the initial nuclide vector or a daughter product of a initial nuclide.

The activity of nuclide i is then

$$A_i(t) = N_i(t)\lambda_i \tag{5.9}$$

and can be derived for all radioactive nuclides.

As the dilution factors for different scenarios are calculated by weather simulations, the activity concentration at some position can be deduced as

$$c_i(t,p,x) = A_i(t) \times D(t,p,x) \tag{5.10}$$

where $D(t,p,x)$ is the dilution factor, and $c_i(t,p,x)$ is the activity concentration of nuclide i, at time t and position p for case x.

5.1.2 Radioactivity measurements of the surrounding air and ground

Instruments such as NaI detectors can be used to identify the decay of radioactive material either in the air or on the ground. To model the response the number of decays of radioactive isotopes from the surrounding during the measurement time of the instrument is needed. The activity concentration $c_i(t,p,x)$ is calculated with equation 5.10. Activity for some given area (if the instrument looks at ground) or volume (if the instrument is looking at the air) is then $A_i(t,p,x) = c_i(t,p,x) \times V$ where V is the area or volume of interest.

The number of decays $\mathscr{N}_i$ for nuclide i during some integration time t_{int} is

$$\mathscr{N}_i = \int_{t_{start}}^{t_{start}+t_{int}} A_i(t,p,x)dt. \tag{5.11}$$

This results combined with the model of the detector setup, and information about the detector efficiency, makes it possible to simulate the instrument response.

5.1.3 Decay and ingrowth for an instrument with collection

The time evolution of nuclides in he case they are collected by an instrument is more complex, as nuclides will continue to decay and be created due to parent-daughter ingrowth during its operation. This requires a more complex model compared to the one describe in the previous section. We investigate two types of instruments: the SAUNA systems, where Xenon is collected from air, and HPGe detectors, where airborne particulates are collected onto a filter. These instruments have three key operational stages:

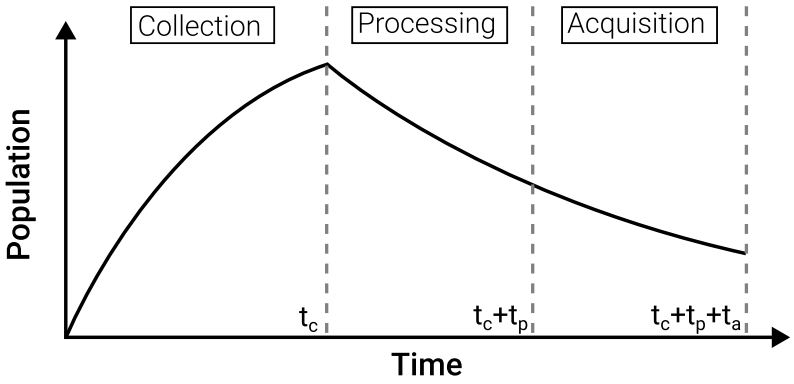

Figure 11: Population with time

- **Collection** for a time t_c, during which nuclides are collected from the air with a constant sampling rate S. Decay and ingrowth continuously occurs among the collected nuclides.
- **Processing** during a time t_p. Collection is at this stage completed, however the measurement by the detector has not yet started. The collected nuclides will continue to decay during this time.
- **Acquisition** during a time t_a. Measurements are performed on the collected sample, and the decays occurring at this point has the possibility to be registered by a detector.

A schematic figure of the population development of a nuclide during these stages can be seen in figure 11.

If the response of these instruments are to be realistically described, each of the stages of the instruments need to be simulated. For the collection phase, equation 5.6 is modified to include a term which describes collection of nuclides. This term depends on the activity concentration $c_i(t)$ [Bq/m^3] of a nuclide in the air (known from equation 5.10), and the sampling rate ϕ [m^3/s] of the instrument. With this addition the population change of nuclide i is described as

$$\frac{dN_i}{dt} = -N_i\lambda_i + \sum N_j\lambda_j B_{ji} + \frac{c_i(t) \times \phi}{\lambda_i} \tag{5.12}$$

where the right term describes the rate of nuclides collected by the instrument. A system of ODEs can be constructed, similar to case in section 5.6, with the modification to the production term as

$$\mathscr{P}_i = \sum N_j\lambda_j B_{ji} + \frac{c_i(t) \times \phi}{\lambda_i}. \tag{5.13}$$

The modeling of the time-dependence of a nuclide collected by an instrument is divided into two distinct phases:

1. **Collection during** $t = 0 \rightarrow tc$ - Nuclides are collected by the instrument. The total number of nuclei of a species, $N_i(t_c)$, collected during t_c, can then be found by solving the system of equations made by equation 5.6 with the production term from equation 5.13, and the initial condition that $N_i(t = 0) = 0$.

2. **Processing and acquisition during** $t = t_c \rightarrow t_c + t_p + t_a$ - After t_c no more nuclides are being collected, however ingrowth and decay continues. The time evolution of the nuclides ($N_i(t)$) can therefore be described by equation 5.6 with the original production term in equation 5.8 between the times $t_c \rightarrow t_c + t_p + t_a$, using $N_i(t_c)$ as the initial condition.

Figure 11 shows the population of a nuclide collected and then allowed to decay in an instrument, indicating the two phases.

The final step to simulate the response of the instruments is to derive the number of decays $\mathscr{N}_i$ during the acquisition interval. From $N_i(t)$ we can find $A_i(t)$. Integrating $A_i(t)$ for the time interval $t_c + t_p \rightarrow t_c + t_p + t_a$ then gives

$$\mathscr{N}_i = \int_{t_c+t_p}^{t_c+t_p+t_a} A_i(t, p, x)dt. \tag{5.14}$$

The integrand is known for all relevant times, and is solved numerically in Python. Detector-specific properties, such as efficiency ϵ, is discussed in sections 5.5 and 5.6.

5.2 Gamma dose rate

Effective dose rate to adult humans from gamma radiation are estimated based on the calculated nuclide-specific activity concentrations in air or on ground. The International Commission on Radiological Protection (ICRP) have published [22] dose rate coefficients that are used here to convert the activity concentrations to dose rate. The nuclide-specific conversion factors are given in units of $\frac{nSv/h^{-1}}{Bq/m^3}$ and $\frac{nSv/h^{-1}}{Bq/m^2}$ for air submersion and ground contamination, respectively.

Given an activity concentration $c_{i,s}(p,t)$ at position p and time t per nuclide i, the effective dose rate $E_s(p,t)$ is calculated by equation (5.15) as the sum over all nuclides, where $e_{i,s}$ is the dose rate conversion factor from ICRP for air submersion ($s = a$) or ground deposition ($s = g$). The total effective gamma dose rate $E(p,t)$ to an adult human standing at p, t is $E_a(p,t) + E_g(p,t)$.

$$E_s(p,t) = \sum_i c_{i,s}(p,t)e_{i,s}; \quad s \in \{a, g\} \tag{5.15}$$

The count rate response of Geiger-Müller (GM) tubes are modelled using the calculated dose rate, scaled with a calibration factor between count rate and dose rate. Using the calculated count rate and the measurement time, Poisson-distributed uncertainty is assumed on the number of measured counts from the tube.

5.3 Radon background model

Decay daughters from radon gas constitutes the dominating background in air sample measurements, and are therefore important to include in the model of the aerosol samplers and the NaI detectors. The two relevant radon isotopes, ^{222}Rn ("radon") and ^{220}Rn ("thoron") are formed as decay products of the uranium and thorium decay series, and their decay products are shown in figure 12.

The early decay products of ^{222}Rn (^{218}Po, ^{214}Pb, and ^{214}Bi) are all short-lived, and will mainly impact measurements made during sampling, for example using a NaI detector monitoring the filter. The later, more long-lived decay products (^{210}Pb, ^{210}Bi, and ^{210}Po) will have some, but normally relatively small, impact on the HPGe measurement of the filter made later.

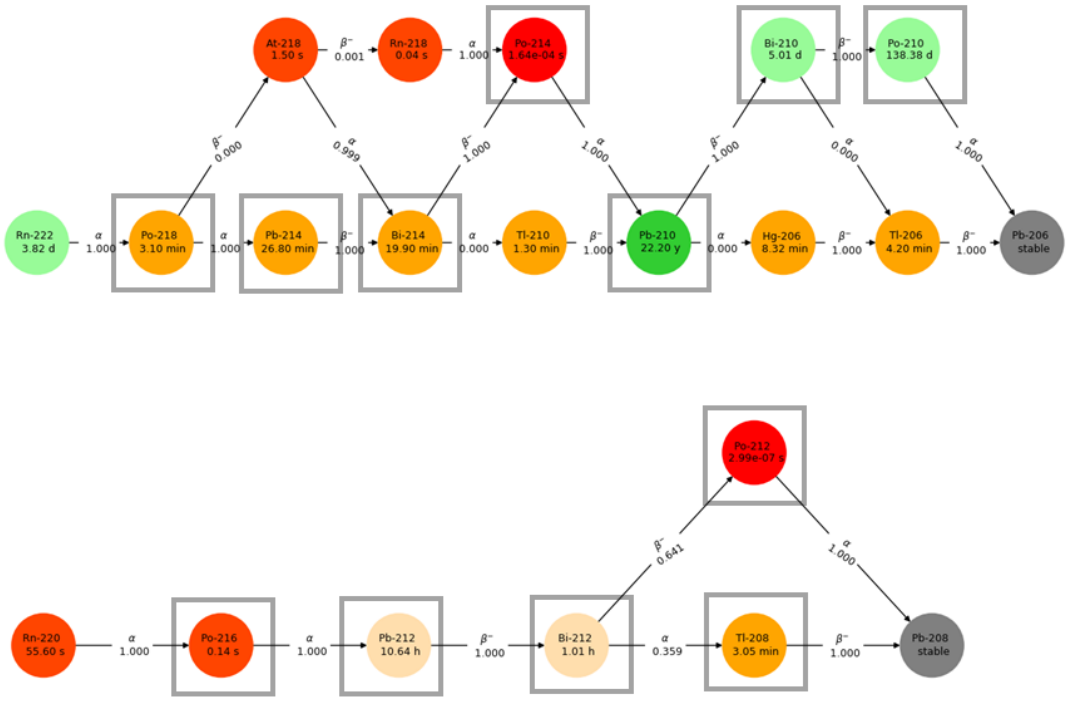

Figure 12: Decay series for ^{222}Rn and ^{220}Rn. The most important daughters are marked with grey squares. The colors indicate different half-life magnitudes; green are long-lived and red are short-lived.

The background originating from thoron is more important for the HPGe measurement, in particular ^{212}Pb, and ^{212}Bi. Even though the filter normally is allowed to decay for one day or more, the relatively long half-life of these isotopes can result in significant peaks in the HPGe spectrum from the filter measurement.

In the model used here, we assumed a constant radon activity concentration of 10 Bq/m^3, and a thoron activity concentration of 0.1 Bq/m^3. These numbers were found to reproduce the average radon daughter activities observed in spectra from the CTBT/IMS station SEX63 in Stockholm, as well as spectra collected in an earlier study using a NaI detector monitoring air sampling filters during sampling [23].

5.4 NaI detectors

The response of sodium iodide (NaI) detectors are modelled using the Geant4 toolkit [24, 25, 26] for the simulation of passage of particles through matter. Two configurations of the NaI detectors are modelled, one configuration where the detector is measuring gamma radiation impinging from the ground and the air around it, and one configuration where it is located behind the collecting filter in an aerosol (particulate-bound radioactivity) collector system.

In both configurations, the Geant4 toolkit was setup to calculate the response of the detectors to emission of mono-energetic gamma radiation from the source (air, ground or filter). The modelled detector estimates the distribution of energy deposited in the detector crystal, per emitted gamma quantum. The response of the detector is thus an energy spectrum of detection efficiency calculated for each gamma-ray with a specific energy emitted from the source.

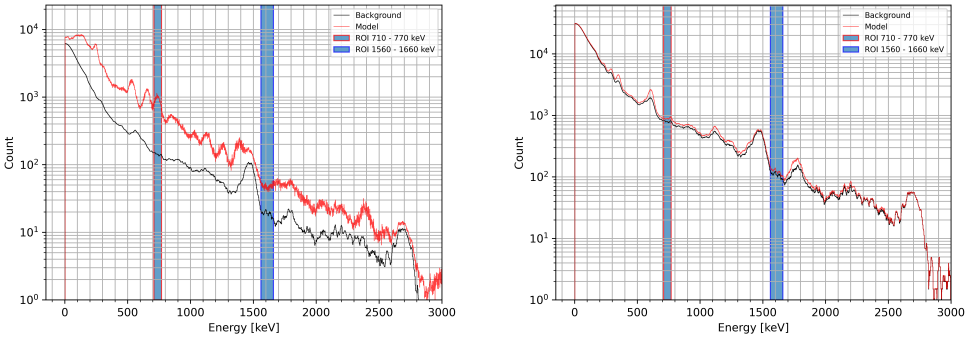

(a) Ground (b) Aerosol

Figure 13: Example of energy spectra and the corresponding background energy spectra produced by the NaI models, measuring activity on the ground (a) and on an aerosol filter (b). The region-of-interests used in the automatic analysis are marked with vertical bands.

This allows the response of the detector to be pre-calculated. Depending on the number of decays per nuclide (see section 5.1), the number of emitted gamma-rays are used to estimate the response of the detector. ENDF/B-VIII.0 data [27] are used to lookup the distribution of emitted gamma-rays per decay of a particular nuclide.

Typical energy spectra produced by the NaI models are displayed in figure 13. The low energy resolution of NaI detectors, as compared to HPGe detectors, complicates the analysis of peaks in the energy spectrum. Some structures in the spectrum are isolated peaks while others may be composed of many overlapping Gaussians. In a real situation, the spectrum would be analyzed with respect to all peaks, but in order to automate the algorithm, we here use a simplified technique, where a list of region-of-interests (ROIs) are defined. Knowing the background used in the model, it is determined if a signal is detected above the background using the framework of Currie [28]. The ROIs were defined as the energy intervals $[710, 770]$ and $[1560, 1660]$ keV, where the signal is assumed to be dominated by gamma radiation emitted from ^{99}Mo and ^{140}La, respectively. The background N_B and signal N_S counts in the ROI is used to estimate the critical limit L_C and MDA using Currie's definitions as used in [29], see equations (5.16), (5.17) and (5.18).

$$L_C \approx 2.33 \cdot \sqrt{N_B} \tag{5.16}$$

$$N_D \approx 2 \cdot L_C + 2.71 \tag{5.17}$$

$$MDA = \frac{N_D}{i\epsilon T} \tag{5.18}$$

Here i is the emission probability of the radiation dominating the signal count in the ROI, ϵ is the detection efficiency of the specific energy and T is the measurement time (live time). The activity A is as estimated using equation (5.19).

$$A = \frac{N_S}{i\epsilon T} \tag{5.19}$$

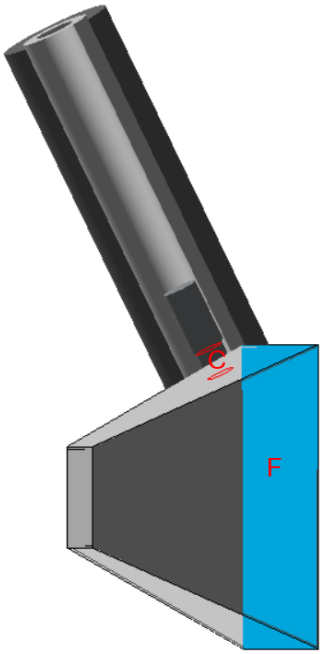

Figure 14: Schematic view of the NaI detector pointing towards the filter in an aerosol system. The NaI detector crystal (C) is positioned inside the red rings. The blue surface indicates the filter (F), collecting aerosols flowing from the right.

5.4.1 NaI detectors in aerosol systems

Aerosol systems can be equipped with for example a NaI detector that measures gamma radiation emitted from the collecting filter (as well as from other sources such as background). Reference [23] describe one such system that was previously used at FOI.

The model for the NaI detector measuring gamma-rays from an aerosol filter is depicted in figure 14. Geometric dimensions and materials used in the model are detailed in Refs. [23] and [30]. The source emitting mono-energetic gamma-rays is the blue filter surface in figure 14, the source is uniformly distributed in the filter and the gamma-rays are emitted isotropically. The photopeak detection efficiency calculated for the model is displayed in figure 15.

5.4.2 NaI detectors in air

The model for the NaI detector measuring gamma-rays from the air around it or from the ground below use the same NaI detector and scintillation crystal as used in the aerosol system (section 5.4.1). The detector in the model is located two meters above the ground as depicted in figure 16. Uniformly distributed, mono-energetic, gamma-rays are emitted isotropically from the ground surface, at zero depth, and the air around the detector. The ground material was assumed to be granite rock. The photopeak detection efficiency calculated for the model is displayed in figure 17. Though no validation data is available for the model, the efficiencies correspond within an order of magnitude to published data of similar setups [31].

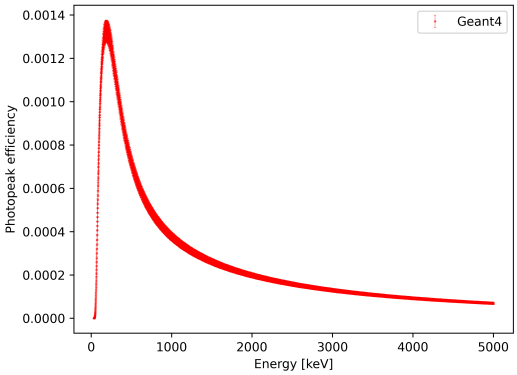

Figure 15: The photopeak detection efficiency vs energy for the NaI detector-in-an-aerosol-system model.

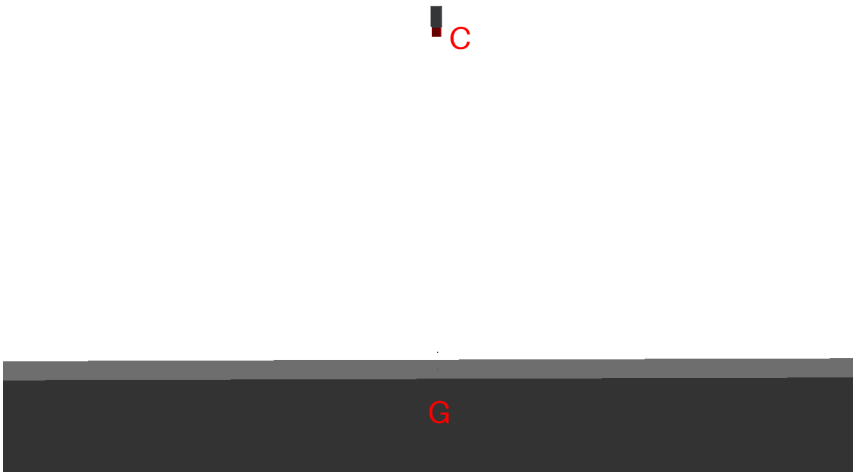

Figure 16: Schematic view of the NaI detector pointing towards the ground (G). The NaI detector crystal (C) is contained in the bottom part of the detector. The distance between the detector and the ground is 2 m.

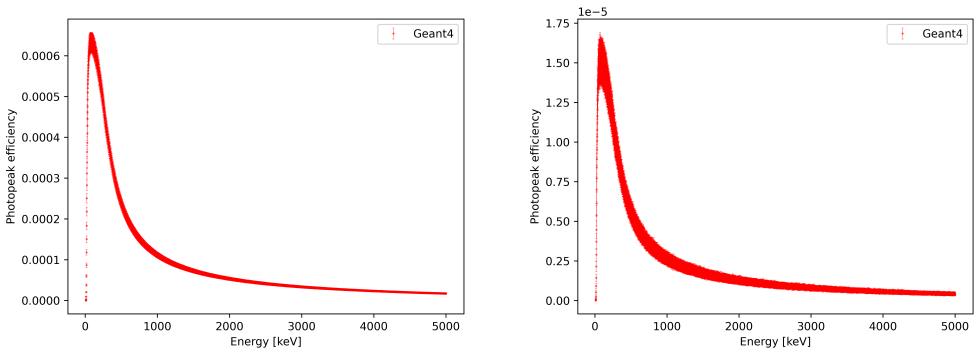

(a) (b)

Figure 17: The photopeak detection efficiency vs energy for the NaI models measuring from (a) the air around it and (b) the ground below it.

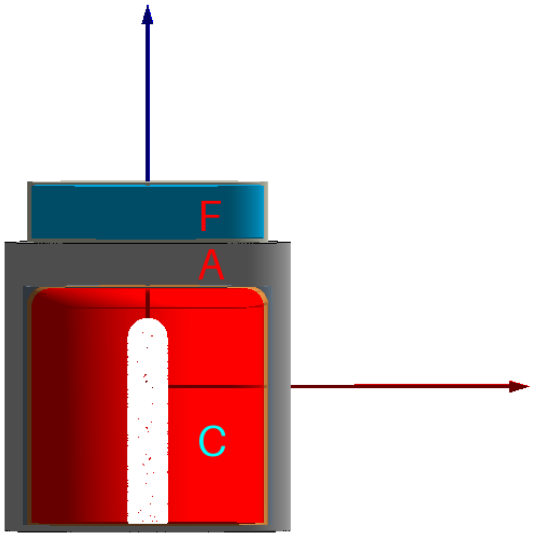

Figure 18: Schematic view of the HPGe detector model. The blue cylinder represents the filter (F) that is the source of gamma radiation measured by the red detector crystal (C) inside the detector aluminium capsule (A). The arrows indicate the reference coordinate system of the detector, with the length of the arrows being 10 cm.

5.5 Aerosol stations

In aerosol stations, radioactive particles are collected by filtering air through filters with high collecting efficiency. Ref. [32] gives an overview of such systems still in use in Sweden. High-purity germanium (HPGe) detectors measure energy spectra from the filters in a shielded environment in a laboratory some time after the sampling have stopped. The response of the HPGe detector measuring on a compressed filter is also modelled using the Geant4 toolkit (as in section 5.4). Figure 18 displays a schematic view of the model.

The isotropic emission of gamma-rays and the energy-spectral response of the detector is the same as described for the NaI detector systems in section 5.4, but with the geometry and materials in the model changed to correspond to this setup.

The photopeak detection efficiency calculated for the model is displayed in figure 19. A validation of the model could be established by comparing the detection efficiency by that from a VGSL [33] model previously setup for the same detector. Figure 19 displays the VGSL results for comparison.

Energy spectra produced by the model for HPGe-based aerosol stations are saved in the IMS2.0 format [34] and evaluated using the UniSAMPO nuclide identification system [35] version 2.67. Peaks in the energy spectrum that are identified and evaluated using UniSAMPO and the corresponding nuclides and their activity concentrations are listed in the response of the station. A typical energy spectrum produced by the HPGe aerosol model is displayed in figure 20.

5.5.1 Comparison between UniSAMPO and model concentrations

UniSAMPO analyse energy spectra and reports on activity concentrations for identified nuclides. To further validate the energy spectral response model of the HPGe detector, the activity contrations calculated by UniSAMPO was

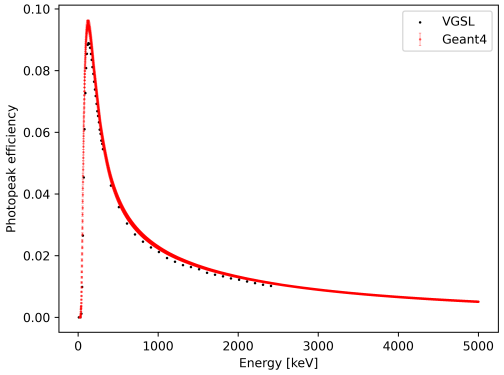

Figure 19: The photopeak detection efficiency vs energy for the HPGe detector model using Geant4. Results from a VGSL model are included for comparison.

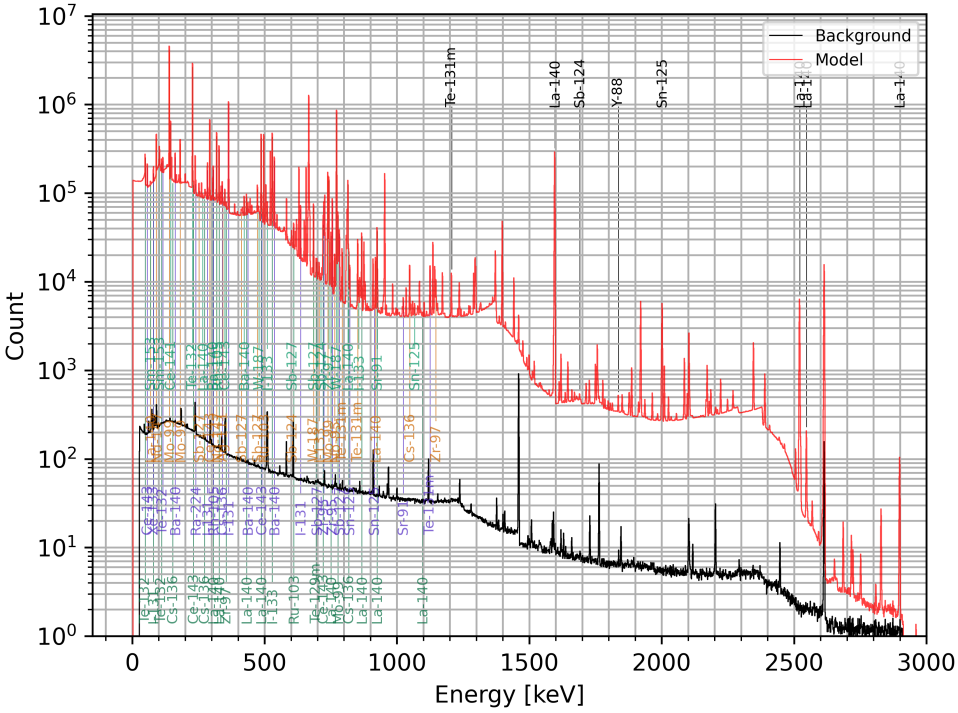

Figure 20: Example of an energy spectrum and the corresponding background energy spectrum produced by the HPGe aerosol model. Peaks identified by UniSAMPO that are also on the list of CTBT-relevant nuclides are marked.

Nuclide	UniSAMPO	Model
Sr-91	0.0089 ± 0.0003	0.007
Y-88	(1.6 ± 0.2)e-05	2.e-09
Zr-95	0.00266 ± 0.00009	0.006
Zr-97	0.0401 ± 0.0006	0.05
Nb-95	0.000414 ± 0.000009	0.0003
Mo-99	0.0790 ± 0.0008	0.09
Tc-99m	0.4 ± 0.1	0.09
Ru-103	0.0120 ± 0.0002	0.01
Rh-105	0.089 ± 0.001	0.1
Ag-111	0.0045 ± 0.0001	0.004
Sn-125	0.00102 ± 0.00004	0.0009
Sb-124	(5.1 ± 0.8)e-05	1.e-05
Sb-127	0.00880 ± 0.00007	0.009
Te-129m	0.0082 ± 0.0002	0.001
Te-131m	0.0112 ± 0.0001	0.02
Te-132	0.0623 ± 0.0005	0.07
I-131	0.0298 ± 0.0003	0.03
I-133	0.0633 ± 0.0008	0.08
Cs-136	0.00079 ± 0.00001	0.0008
Ba-140	0.0257 ± 0.0002	0.03
La-140	0.0529 ± 0.0003	0.02
Ce-141	0.0106 ± 0.0002	0.01
Ce-143	0.0481 ± 0.0005	0.07
Nd-147	0.0142 ± 0.0002	0.01
Sm-153	0.0075 ± 0.0003	0.008

Table 4: Activity concentrations in Bq/m^3, for CTBT-relevant and particulate bound nuclides as reported by UniSAMPO and the corresponding input used by the model for the case described in section 8.

compared to the model activity concentration input, calculated from the assumed release and collected at the filter. Table 4 displays the data used for the comparison, for the same example case as used in section 8 for CTBT-relevant particulate bound nuclides. The relative differences between the numbers listed in table 4 are for many nuclides within the statistical uncertainties, albeit with some notable exceptions where a higher difference is noted, e.g. Y-88, Zr-95, Tc-99m and Te-129m. Considering the many steps in the modelling chain and associated uncertainties, the comparison in table 4 indicate that, for this case, the energy-spectral detector response modelling framework does not add uncertainties that are expected to dominate the uncertainties of the complete model, e.g. the atmospheric transport models are expected to introduce uncertainties larger than the differences displayed here.

5.6 Radioxenon systems

The responses of two types of radioxenon systems are modelled; the SAUNA III and the SAUNA Q_B, which both performs ultra-sensitive measurements of the four radioxenon isotopes ^{131m}Xe, ^{133}Xe, ^{133m}Xe, ^{135}Xe. These system are from the same product family, however, with key differences in collection time, size and price. The state-of-the-art system SAUNA III has a collection time of six hours, and used by CTBTO to monitor radioactive Xenon in the atmosphere. The SAUNA Q_B is a physically much smaller system, with a collection time of twelve hours. At a lower price-point than SAUNA III it can

	SAUNA Q_B	SAUNA III
t_c [h]	12	6
t_p [h]	3	5.3
t_a [h]	10.7	6.2
ϕ [m^3/h]	1.2	4

Table 5: The instrument parameters used in the modelling.

	Branching ratio (B)	Half life	Detection efficiency (ϵ)
^{131m}Xe	0.352	11.93 d	0.65
^{133}Xe	0.465	5.24 d	0.65
^{133m}Xe	0.35	2.19 d	0.65
^{135}Xe	0.47	9.14 h	0.65

Table 6: Parameters for the xenon isotopes used in the modelling.

be used a compliment or in an array configuration. A five-unit SAUNA Q_B array is operated by FOI in Sweden since 2022.

The two system types use the same main principle: air is collected during a collection time of 6 or 12 hours, followed by xenon extraction and purification and then the activity of the sample is measured by a β-γ coincidence detector. An overview of the important steps in modelling is described here, for a in-detail description see [36], [37] and references therein.

5.6.1 Modelling the detection response of a radioxenon system

As is described in section 5.1.3, the SAUNA systems will collect air during t_c, after which there are some processing time t_p and finally measure the activity during the acquisition time t_a. With equation 5.14 we can model how many counts $\mathcal{N}_i$ that occurs in a collected sample during the acquisition time for a radio-xenon isotope i. To model the statistical variation of the measurements, $\mathcal{N}_i$ is randomized using a Poisson distribution. $\mathcal{N}_i$ is then used to calculate the activity concentration if it was measured by a SAUNA system, $c_{i,M}$, as

$$c_{i,M} = \frac{\mathcal{N}_i}{\epsilon B_i} \frac{\lambda_i^2}{(1-\exp(-\lambda_i t_c))\exp(-\lambda_i t_p)(1-\exp(-\lambda_i t_a))} \frac{1}{\phi} = \frac{\mathcal{N}_i}{S_i}, \quad (5.20)$$

where ϵ is the detection efficiency, B_i is the branching ratio, λ_i is the decay constant and ϕ is the airflow. Equation 5.20 assumes that the activity concentration is uniform for the Xenon isotopes during the collection time t_c. The instrument properties used in the model are shown in Table 5 and the xenon istope properties are shown in Table 6. A parameter S_i is defined, relating the activity concentration to net-counts measured in the detector.

The decision limits critical limit (LC) and minimum detectable concentration (MDC) can be calculated as

$$LC_i = \frac{k_\alpha}{S_i}\sqrt{var_0(\mathcal{N}_i)} \quad (5.21)$$

$$MDC_i = \frac{1}{S_i}(k_\alpha^2 + 2k_\alpha\sqrt{var_0(\mathcal{N}_i)} \quad (5.22)$$

where a 95% confidence level is set by $k_\alpha = 1.654$, and $var_0(\mathcal{N}_i)$ is the variance of $\mathcal{N}_i$, which can be calculated according to Eq. (B.2)-(B6) in Appendix B of [37].

6 Simulations of responses from seismic sensors

6.1 Introduction

In this work, the goal of the modelling of the seismic network response is to provide a relatively simple simulation that still can be used to provide information on key parameters for network design. The model is based on previously published studies of the detection capability of the global International Monitoring System (IMS), in particular the ones presented in Refs. [38] and [39]. Here we use a similar, somewhat simplified, approach for a regional network. As discussed in more detail in this section, the model has several limitations, but we consider it adequate enough for its purpose, which is to estimate the detection- and location capability for the cases discussed in section 2.3, and to feed key parameters into the aggregated system model. The modelling of the seismic detection capability is described in the next section, followed by the location uncertainty modelling in section 6.3.

6.2 Modelling of the detection process

Simulations of detection capability from seismic networks is typically based on a statistical model of the noise at the stations and a modelling of the seismic signals [39], see also Ref. [40] for a more elaborate model example. The ambient seismic background noise for a particular station will depend on the location as well as the number of detection elements at the station. In general, two types of stations are used, seismic arrays and single-element stations - both equipped with three-component sensors. A seismic array is comprised of a set of seismometers placed in a configuration that allows for the seismic wave to be coherent among the different seismometers in the array. This allows for an analysis technique called "beamforming", where the individual signals are time-shifted and added, which will reduce the ambient background and amplify the signal. Arrays can also be used to estimate the direction to the seismic event (its azimuthal angle) and the apparent velocity of the signal; however, this capability is not modelled here.

An nuclear or chemical explosion will cause both compression (P) and, to a lesser extent, shear, or transverse, (S) seismic waves that will propagate in the earth's interior. In addition, surface waves are created. P waves are the first to arrive at a measurement station, followed by S waves. Surface waves arrives after the P- and S-waves. In this work, we use only P-waves. For an explosion with a given yield, the magnitude as determined from P-waves, m_b, is estimated according to

$$m_b = 4.43 + 0.75 \times log_{10}(w) - D(h), \tag{6.1}$$

where w is the explosion yield in kilotons (kt) and D is a decoupling factor which depends on the height or depth of burial of the explosion, as well as on the surrounding media. This empirical relationship (not including D) was created using data from the former Soviet underground nuclear test site in Semipalatinsk [41]. The seismic coupling also changes with the geological conditions and if any action has been taken to actively decouple the explosion, for instance by placing the device inside an existing underground cavity. None of these two factors are taken into account here. The seismic coupling of an

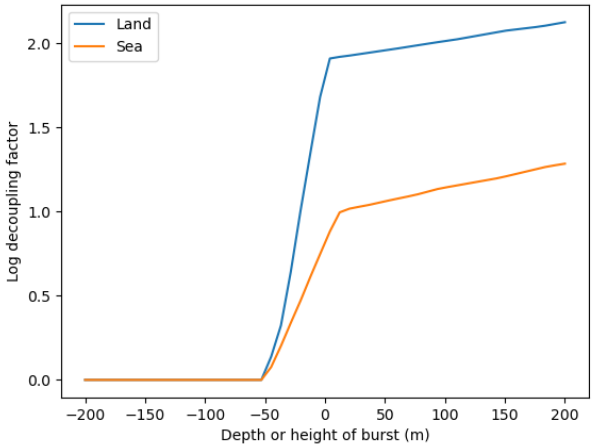

Figure 21: Magnitude correction factor for decoupling obtained from Ref. [38].

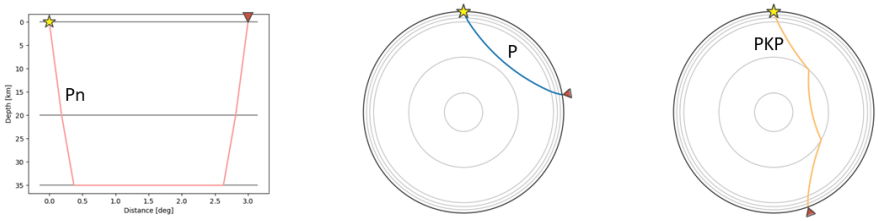

Figure 22: Left panel: A Pn wave travelling along the boundary between the crust and the upper mantle (Moho) at shorter distances. Middle panel: A P wave in the teleseismic zone. Right panel: A PKP wave travelling the outer core.

explosion conducted above, or in, seawater will be stronger compared to land. The magnitude correction factor $D(h)$ is obtained from Ref. [38], and shown in figure 21.

The resulting amplitude, A, of the signal in a seismometer is modelled by

$$log_{10}\frac{A}{T} = m_b - C(d), \tag{6.2}$$

where T is the dominant period of the investigated seismic signal and C is a distant-dependent correction term, adjusting for the fact that the transfer function for seismic waves is strongly affected by earth's inner structure.

Earth's layered structure will create different P- and S trajectories (phases), and depending on the distance between a station and the source, different focussing and shadow zones are created. A regional zone up to about 10° result in P waves passing through the crust and the upper mantle, resulting in Pg and Pn phases. A shadow zone is observed between 10° and 20° caused by wave refraction into deeper layers. A teleseismic zone with more reliable detection possibilities spans between 20° and 100°, and another shadow zone is found between 100° and 140°. Finally, a zone with P waves passing through the outer and inner core (PKP phases) will again provide higher detection possibilities (see figure 22).

The model uses the m_b correction curve $C(d)$ reported in Ref. [39], which spans distances of 0° to 180° for a near-surface explosive source. The correction

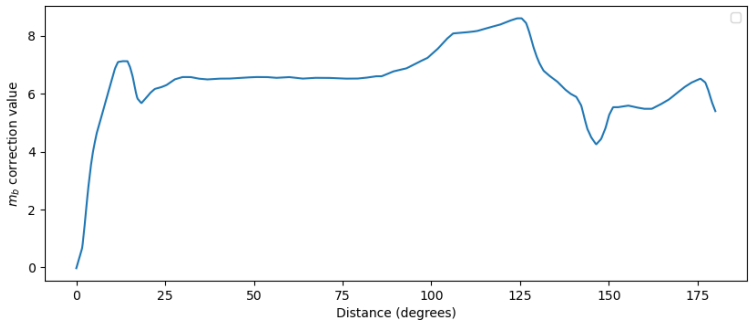

Figure 23: The distance-dependent m_b correction curve used in this report, obtained from Ref. [39].

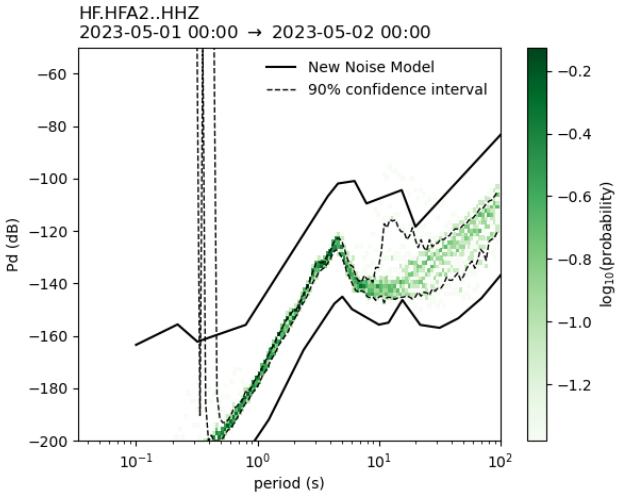

Figure 24: Example of a displacement power spectral density function from one of the elements in the Hagfors station used to calculate the statistical noise level used in the model. P_d was read at a center frequency of 1.33 Hz ($T = 0.75$ s).

thus includes both the regional (Pg, Pn), teleseismic (P), and PKP phases above 100°. The distance-dependent correction is shown in figure 23.

The amplitudes caused by an explosion scenario as a function of distance from the explosion is calculated by combining equation 6.1 and 6.2. For the seismic wave to be detected by a seismograph it is required that the signal exceeds the ambient statistical noise recorded at the station with a certain amount, *i.e*, the signal-to-noise ratio (SNR) should exceed a chosen detection threshold value. The statistical noise, D, for a single seismometer was obtained by using the typical noise levels observed at the Swedish seismological array in Hagfors (HFS).

The noise parameter was calculated by an averaging of typical dB readings from displacement power spectral density (PSD) functions from all elements in the Hagfors array, and converted to displacement i nm. An example PSD function from the Hagfors array is shown in figure 24. The displacement was calculated using upper and lower corner frequencies of 0.8 and 2.2 Hz, respectively, corresponding to the typical frequency range for P- and PKP waves [39]. This resulted in a RMS displacement of $D = 0.59$ nm from noise in the P-wave

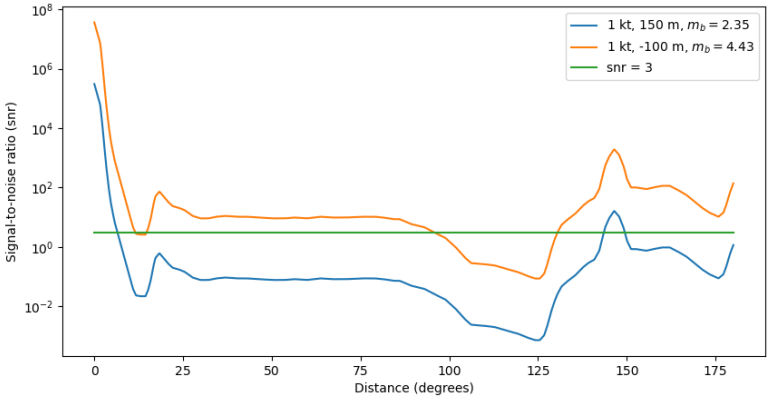

Figure 25: Signal-to-noise ratios for two explosion scenarios plotted versus source-station distance. The green line indicates $SNR = 3$, which is the threshold value required for detection in this model.

frequency band[1]. The same noise level is used for all stations in the model. The noise reduction obtained by using a seismic array is estimated by,

$$D_{array} = \frac{D}{\sqrt{N}}, \tag{6.3}$$

where N is the number of array elements. The same approach is used in Refs. [38] and [39]. In this work, an explosion is assumed to be detected if the signal-to-noise ratio is equal to or larger than 3.

The resulting SNR, defined as A/D or A/D_{array} for single or array stations, respectively, is shown in figure 25 for two explosions. In one case, a 1 kt device was detonated underground, resulting in $m_b = 4.4$. This corresponds, roughly, to the first nuclear test in North Korea in 2006. Such an explosion would according to this model be detected at all distances, except for a narrow region around 15° and the shadow zone between 100° and 130°. If instead the explosion was conducted at an altitude of 150 m above land, the magnitude would be reduced to 2.3, and the explosion would be detected only at distances less than about 6°, and in a narrow region slightly within 150°.

The detection model was evaluated using IMS data from the screened event bulletin (SEB) produced by the International Data Center (IDC) for CTBT monitoring. Magnitudes (m_b and ML [2]) for all events that included the Hagfors station in the analysis were plotted versus distance from the Hagfors station and compared to the detection threshold predicted by the model, see figure 26.

As can be seen in the figure, the predicted detection threshold for the complete array agrees reasonably well with the lowest observed values, with the exception of a region around 15° and one at 140° - 150°. A similar study reveals the same features for other IMS stations [39]. In this work they explain the discrepancy at 15° by the interstation distance in the IMS network, and the discrepancy at 140° - 150° by the way the IMS stations are associated in the analysis (see Ref. [39], section 5, for details).

[1] The average noise at the nine elements in the Hagfors array is measured to $P_d = -186$ dB $= 2.51 \times 10^{-19}$ m^2/Hz for the center frequency $f_0 = \sqrt{f_u \times f_l} = 1.33$ Hz, where $f_u = 2.2$ Hz, and $f_l = 0.8$ Hz. The resulting RMS displacement is $D = \sqrt{P_d \times (f_u - f_l)} = 0.59$ nm

[2] The IDC calculates local magnitudes for shallow events using only P and P_n phases (to make them consistent with m_b) recorded at stations located within 20° from the event [42].

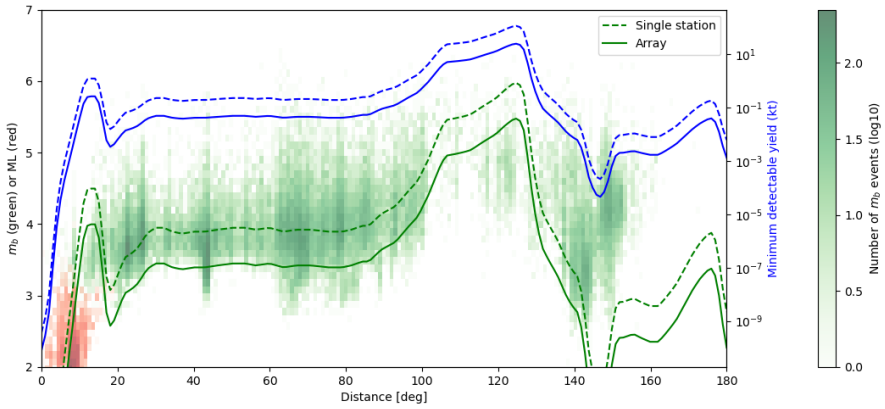

Figure 26: A comparison of modelled detection threshold magnitudes for the Hagfors station (green lines, left vertical axis) and magnitudes (m_b as green and local magnitude ML as red histograms) reported by the IDC where Hagfors is included in the analysis. Data is from the Screened Event Bulletin (SEB) for 2018-2022. The solid green line is the threshold magnitude for the complete array (nine components), and the dotted line is the threshold magnitude for a single component. The corresponding threshold for the explosive yield of a fully coupled explosion is also shown (blue lines, right vertical axis).

6.3 Modelling of the event location capability for a seismic network

The localization of a seismic event is here performed by finding the minimum of the summed difference between modelled observed arrival time and the arrival time calculated from assumed event time and location,

$$r = \sum_{i=1}^{n} \left(\frac{t_i^o - t_i^c}{\sigma_i} \right)^2 . \tag{6.4}$$

Here, n is the number of detected phases, which in this model (using only P-waves) is equal to the number of stations included in the location, and t_i^o and t_i^c is the observed and calculated arrival times, respectively. The arrival time error is denoted by σ_i.

The calculated arrival time is

$$t_i^c = T(d_i) + t_0, \tag{6.5}$$

where $T(d_i)$ is the travel time model used, d_i is the geodesic distance between the station and the assumed event location, and t_0 is the assumed event time. The observed arrival time is modelled as

$$t_i^o = T(d_i^{true}) + t_0^{true}, \tag{6.6}$$

where *true* denotes the actual time and location for the explosion. The difference between observed and calculated arrival times is achieved by perturbing the measured arrival times with an uncertainty taking into account pick time error and a model error according to

$$\sigma_i^2 = 0.75^2 + \left(\frac{0.15}{SNR_i - 1} \right)^2 , \tag{6.7}$$

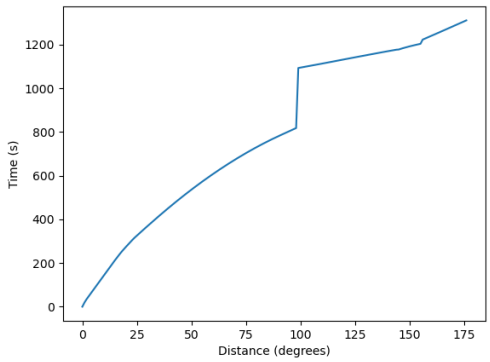

Figure 27: The seismic signal travel time model used in this report.

where the first term is the model error, and the second is the pick time error. The approach is the same as used in Ref. [38]. This simple model should be considered a first-order approximation. Nevertheless, it results in reasonable agreement with the location accuracy achieved for events inside the Swedish National Seismic Network (SNSN), as will be illustrated.

The travel time model, $T(d)$, is based on the work by Kennet and Engdahl [43]. Travel times for different P phases that might be present at different angular distances (P, PKIKP, PKiKP, and PKP) are combined to create a single travel time table up to a distance of 180°. The resulting travel time function (see figure 27) is similar to the one used in Ref. [38]. It should be noted that the specifics of the travel times will not significantly affect the results on location in the model since the arrival time uncertainty (equation 6.7) is only weakly dependent on travel time through the factor involving the SNR parameter.

The minimum of the residual in equation 6.4 is found by performing a grid search within a 600×600 km area with a spacing of 2.5 km. The geographical location of the minimum in the resulting 2D distribution is found by calculating the centroid of a contour polygon. The localization procedure is performed for 100 Monte Carlo histories assuming that the observed arrival time is normally distributed with a standard deviation of σ_i as determined from equation 6.7. Finally, the 90% error ellipse is calculated from the resulting distribution. The model requires at least four detecting stations in order to perform an event localization. An example of a model location result is shown in figure 28.

To investigate the realism of the outlined model, it is compared to real events measured and analyzed by SNSN [44]. Global and national seismic events detected by SNSN was modelled and located using the same stations as in an analysis with the SeisComP analysis software [45]. The latter analysis was carried out with manual picking of P-phases, or P- and S-phases, and using the LOCSAT localization module [46]. The model was found to agree reasonably well with the more sophisticated SeisCompP analysis, resulting in comparable confidence ellipses, as illustrated in figure 29. For these examples, the model resulted in location uncertainties slightly larger than the P+S LOCSAT results, and smaller than the P-only results. Obviously, it is not to be expected that the model should agree well in all cases, or for all distances, given its simplicity. But we consider the model to be adequate enough for its purpose, *i.e.*, to facilitate a relative comparison of the location capability for different network designs.

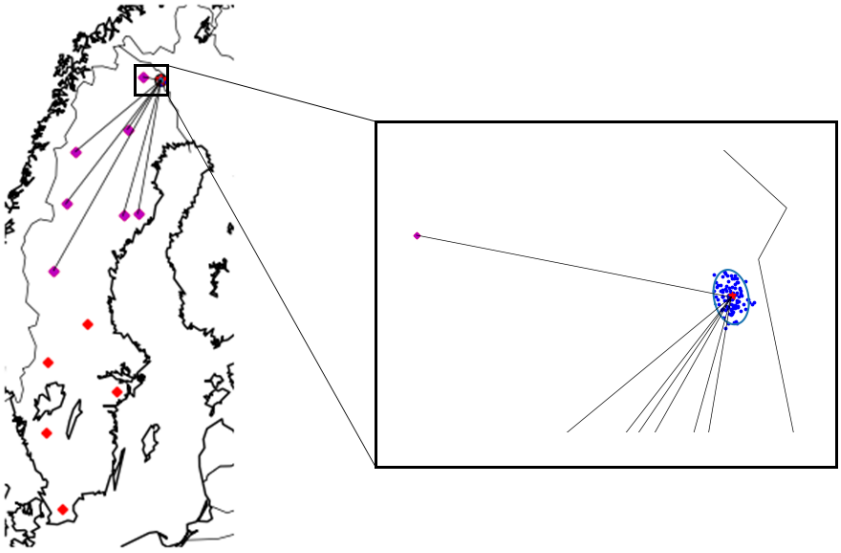

Figure 28: Example of a modelled location using a fictitious seismic network in Sweden. The confidence ellipse is calculated using the resulting event location distribution obtained from Monte Carlo of the modelled arrival time uncertainty (100 histories). The location estimate for each history is performed by grid search. The models resulted in this cas in a one sigma uncertainty of about 5 km for both latitude and longitude.

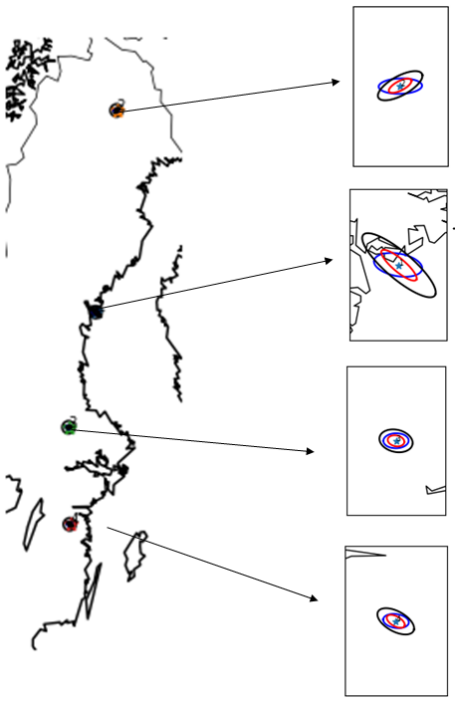

Figure 29: Examples of comparisons between 90% confidence uncertainty ellipses created using the model presented in this report (in blue) and real data analysed using SeisComp with the LOCSAT module. Data was analysed with manual picking of P-phases only (in black), and using both P-and S phases (in red).

7 Simulations of responses from infrasound sensors

7.1 Introduction

The modelling of the infrasound response is to a large extent based on the work reported in Ref. [38]. Just as in the seismic model, described in chapter 6, the intention here is to estimate the average detection and location capability by exposing different network configurations to a set of hypothetical nuclear explosions, and feed key parameters into the aggregated system model. The modelling of the detection capability is described in the next section, followed by the location modelling in section 7.3.

7.2 Modelling of the infrasound detection process

A nuclear explosion in the atmosphere will produce an acoustic signal that will travel large distances (thousands of km) due to refraction in different atmospheric layers at high altitudes (up to more than 100 km). The energy of these waves is concentrated around frequencies between 20 and 500 mHz. Sound with frequencies below 16 Hz is called infrasound, and can be detected by low frequency microphones or microbarographs. The direction to the source (bearing) can be calculated using an array of several sensors, and event location can be estimated using a station network.

Since the wind speed at high altitudes can be up to 100 m/s, *i.e.*, a significant part of the speed of sound, the wind conditions will affect the motion of the wave, and also have an impact on the localization of the event.

The infrasound detection process is modelled using essentially the same empirical approach as described in Ref. [38]. Using data from nuclear and large conventional explosions, it has been found that the signal amplitude, or pressure difference, P, measured in microbars at a distance of r in km from a 1 kt atmospheric explosion, can be estimated using the relation,

$$P = 29374\sqrt{Y}r^{-1.349}, \tag{7.1}$$

where Y is the *effective yield*, which depends on the height of the explosion. As can be seen in figure 30, the effective yield can be considerable larger than the true yield. At a height of about 300 m, the effective yield for a true yield of 1 kt is about 6 times higher. Note also that the curve in figure 30 also have data for partly buried explosions. In fact, infrasound signals also have been observed from underground nuclear tests, see for example Ref. [47]. Data indicates that wave reflections in the 50 km atmospheric layer will be the strongest for waves created in explosions, and according to Ref. [38], equation 7.1 is believed to represent these stratospheric phases.

As mentioned above, the wind speeds at high altitudes can have a significant effect on the infrasound wave propagation. The average wind velocity vector V along the signal trajectory is used to correct the signal amplitude by a factor W given by Ref. [48]

$$W = 10^{0.0173V}. \tag{7.2}$$

Positive values of V indicates that the signal is travelling downwind, which will result in an amplification of the infrasound signal, and weaker signals for negative values.

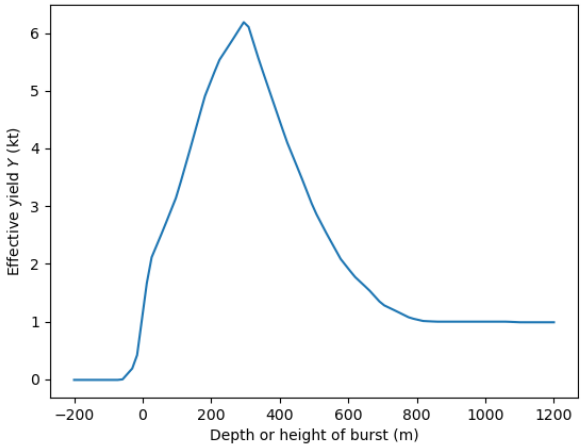

Figure 30: Effective yield for the infrasound signal from a 1kt nuclear explosion (obtained from Ref. [38]).

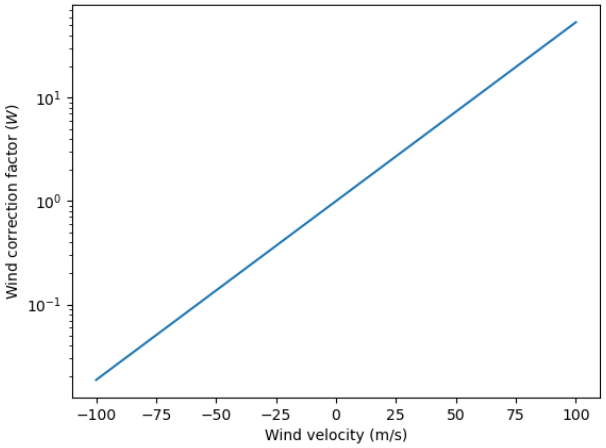

Figure 31: Multiplicative signal amplitude correction factor as a function of wind velocity.

As can be seen in figure 31, this correction can be large if the winds are strong, and result in significant damping or amplification of the signal. To calculate this effect, we use monthly averaged wind field data [49], and calculate the average wind vector along all event-station trajectories at a constant pressure of 0.7 mbar, which roughly corresponds to an altitude of 50 km. Data is illustrated in figure 32, where the monthly average wind fields for 2018 are shown. As can be seen, the mean winds at this altitude vary strongly with season. In January for example, Europe is dominated by strong westerly winds, causing a low infrasound detectability for sources east of Sweden. In the summer, easterly winds instead are dominating. The variation is further illustrated in figure 33.

The measurements of a microbarometer will also be affected by noise from local winds at surface level. We use the same modelling of the noise as in Ref. [38], i.e.,

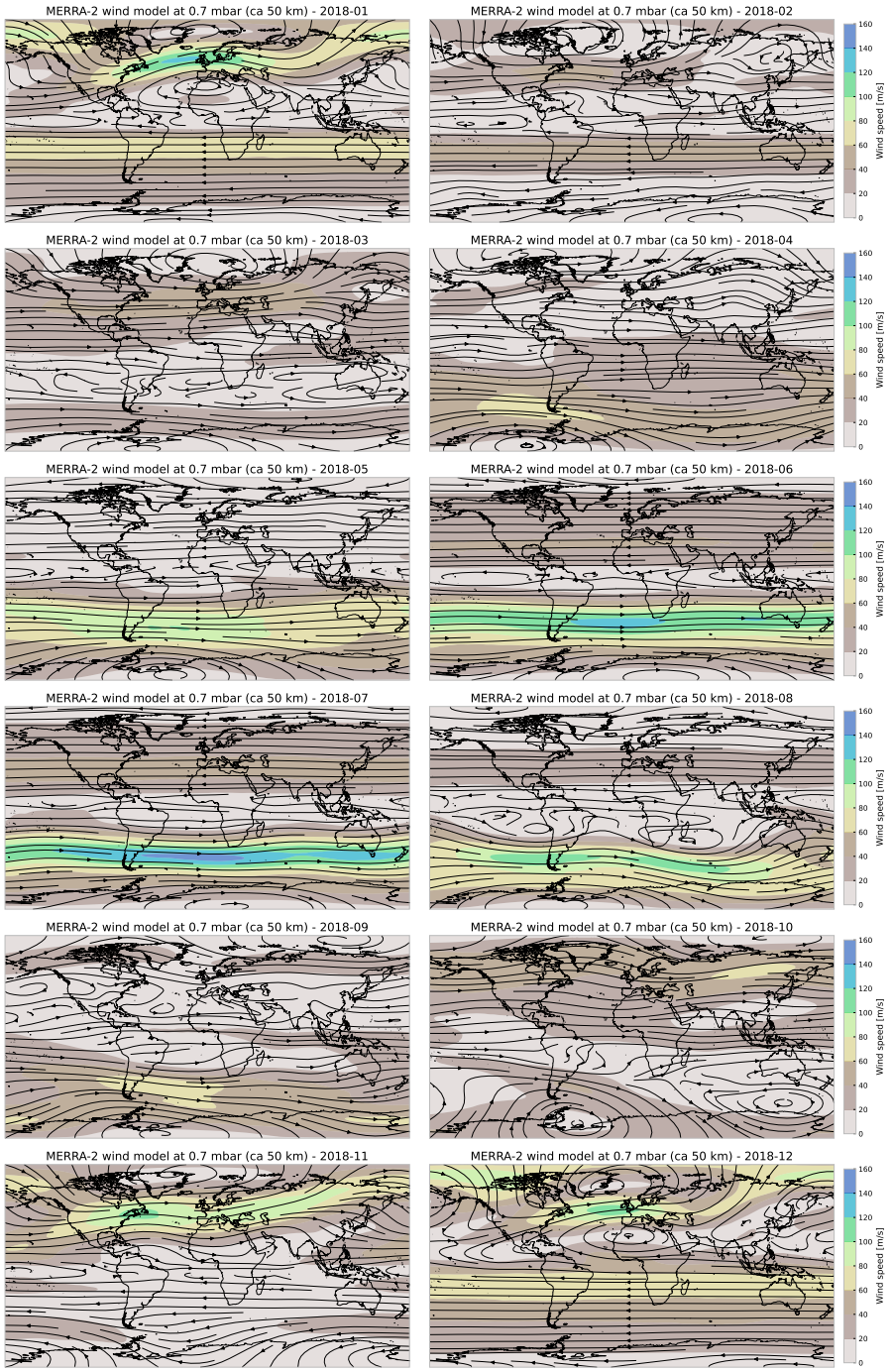

Figure 32: Monthly averaged wind field data during 2018, at a constant air pressure of 0.7 mbar, which approximately corresponds to an altitude of 50 km [49].

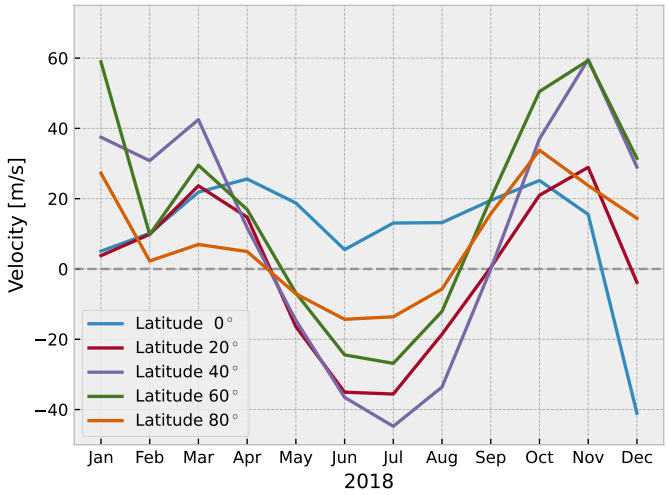

Figure 33: Monthly averaged wind velocity at 50 km altitude above the equator and at four different latitudes at the northern hemisphere. Data was obtained from Ref. [49].

$$N = \begin{cases} 0.4v, & \text{if } v < 5 \text{ m/s} \\ 0.035v^{2.5}, & \text{otherwise,} \end{cases} \tag{7.3}$$

where v is the local wind speed and N is the 1σ wind noise in microbars. Also for the local winds we use monthly averages [50].

7.3 Modelling of the event location capability for an infrasound network

An infrasound station detecting a signal will produce a bearing and an arrival time which together with other stations can be used to estimate the location of the source by triangulation of multiple station intersections and some model to combine arrival times and bearing. In this report, we estimate the location uncertainty area with a simple intersection polygon area in the case of two detecting arrays, assuming an uncertainty in the bearing measurements.

In the case of three or more detecting stations, we perform a grid search, of the same kind as described in section 6.3, but this time also including information on the measured bearing and calculating a residual at each grid point according to

$$r = \sum_{i=1}^{n} \left(\frac{t_i^o - t_i^c}{\sigma_i^t} \right)^2 + \sum_{i=1}^{n} \left(\frac{\theta_i^o - \theta_i^c}{\sigma_i^\theta} \right)^2, \tag{7.4}$$

where, as in section 6, t_i^o and t_i^c is the observed and calculated arrival times with uncertainty σ_i^t, and corresponding notation for the bearing θ. Since the residual is error-weighted, it becomes dimensionless, making it possible combine time and bearing in the same residual. The process is repeated for 100 trials assuming a normally distributed arrival time uncertainty of σ_i^t calculated as 2% of the travel time. The travel time is modelled as $d_i/0.3$ km/s, where d_i is the distance from the event to the station. The distance dependent bearing uncertainty is given by

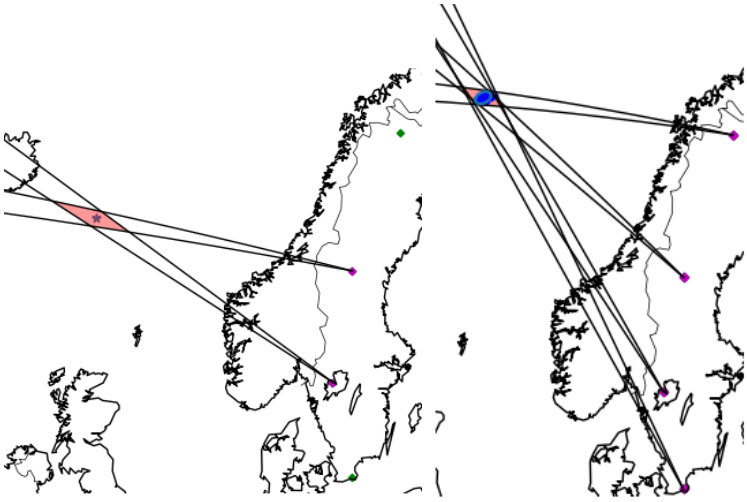

Figure 34: Examples of infrasound locations using a fictive four-station network in Sweden. In the case of two detecting stations, the event location is performed using the intersection of the to bearings, and the area of uncertainty is taken as area of the resulting polygon (left panel). In the case three or more stations detect the event, a 90% confidence ellipse is created using Monte Carlo of the bearing and arrival time uncertainty distributions (right panel).

$$\sigma_i^\theta = \begin{cases} 1.8^\circ \text{ if } d < 3000 \text{ km}, \\ \text{lineary increasing from } 1.8^\circ \text{ to } 7.1^\circ \text{ between } d = 3000 \text{ and } d = 4000 \text{ km}, \\ 7.1^\circ \text{ for } 4000 < d < 10000 \text{ km}, \\ \text{lineary increasing from } 7.1^\circ \text{ to } 27.5^\circ \text{ between } d = 10000 \text{ and } d = 15000 \text{ km}, \\ 27.5^\circ \text{ for } d > 15000 \text{ km}, \end{cases} \tag{7.5}$$

where d is the great circle distance from the station to the event.
Two examples of event localization are shown in figure 34.

8 Example of results

8.1 A hypothetical network

In this section, we discuss how NEMOS is used to analyze a fictitious test network in Sweden, shown in figure 35. This network is not a part of any design study; it is only used as an illustration of the software functionality. The network consists of 12 seismic and four infrasound stations, 10 GM tubes, and one multi-detector radionuclide site equipped with an aerosol station with an HPGe detector and an additional NaI detector monitoring the filter during air collection, one stand-alone NaI detector, one GM-tube, and two noble gas systems (SAUNA Q_B and SAUNA III).

The network was investigated using explosion sets A, B, BW, and C, described in section 2.3, using a nuclear source term assuming a 1 kt nuclear explosion. Both aerosol (air and ground deposition) and noble gas atmospheric transport calculations were used to simulate the radionuclide signal. The particle dispersion model, described in section 4.2, assumed an explosion height of 150 m, while the noble gas model assumed a point source at 100 m. The differences are due to the fact that at present, we don not have access to a proper model for dispersion of noble gases from an atmospheric nuclear explosion, and we used a standard model normally used to simulate underground explosions. As a consequence, the results for particulates and radioxenon are not fully comparable. The intention is to develop a more elaborate model for noble gases in the future.

8.2 Response from seismic and infrasound subnetworks

The resulting detection capability of the seismic and infrasound subnetworks is illustrated in figure 36, for explosion set C. For a seismic event to be detected, we require at least four stations detecting the event. For an infrasound station, two detecting stations are required. As can be seen, there are notable, and expected, differences in detection capability between the two measurement technologies. The seismic detection capability is clearly affected by the fact that the seismic coupling is stronger if the explosion occurs above water, resulting in considerably larger detection distances in those cases. Infrasound signals, on the other hand, can in this case be detected at larger distances, but are affected by high-altitude wind patterns. This effect causes a generally decreasing detection capability for explosions east of the hypothetical network, due to, dominating westerly winds. However, this effect varies depending on the season.

Results for localization capability are shown in figure 37, where the seismic and infrasound location area uncertainties are compared for case C (Europe). Only events where both techniques could locate the event are included. As can be seen, the location area is, as expected, in many cases at least an order of magnitude larger for the infrasound network.

8.3 Response from GM-tubes, NaI- and aerosol sampling

To illustrate the individual responses from GM-tubes, NaI detectors, and aerosol collection systems, we use results from one of the explosions (number A378) in explosion set A that resulted in detections. An example of measured dose rate using a GM tube is shown in figure 38. In this case the GM-tube at the

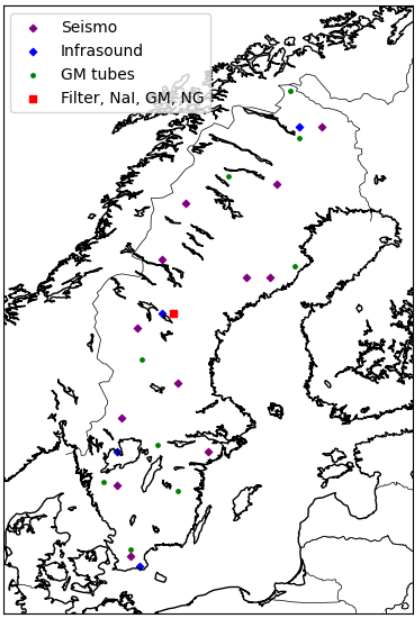

Figure 35: Layout of the hypothetical detection network used to exemplify results. The network is equipped with 12 seismic and 4 infrasound stations, 10 GM-tubes and a multi-sensor radionuclide station containing a filter station with HPGe detector and a NaI-detector, a stand-alone NaI detector, and two noble gas systems (one SAUNA III and one SAUNA Q_B.

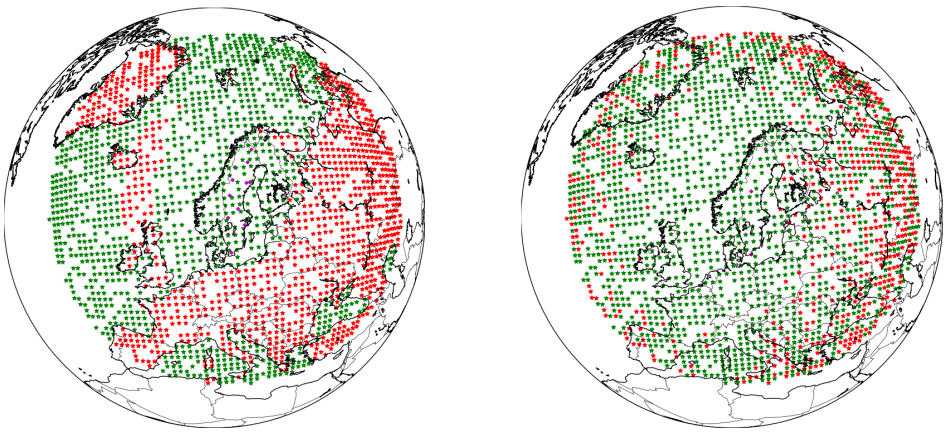

(a) Seismic detection pattern (b) Infrasound detection pattern

Figure 36: Seismic (left panel) and infrasound (right panel) detection patterns for set C using the hypothetical network shown in figure 35. Green stars indicate that the explosion was detected by the subnetwork. Explosions that were not detected are shown as red stars. Station locations are indicated by purple diamonds.

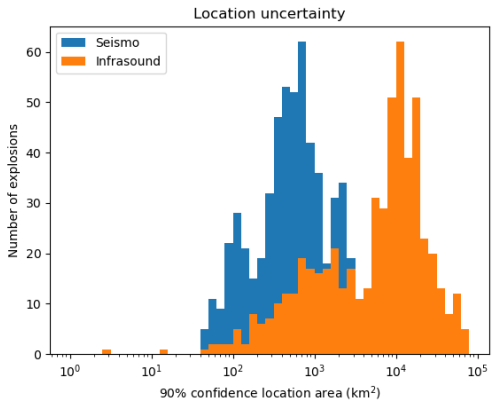

Figure 37: Distributions of uncertainties in location area for case C for the seismic and infrasound networks in the example network.

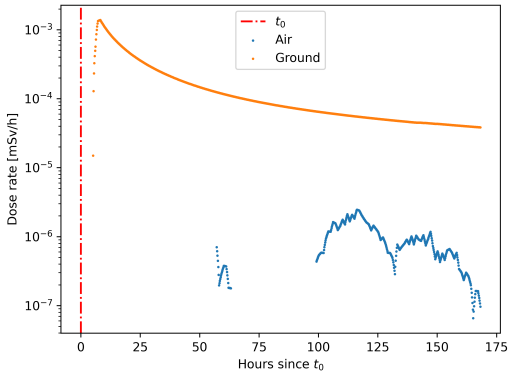

Figure 38: Example of the measured dose rate as function of time since explosion for a detecting GM-tube (explosion A378). The dose rate is calculated every hour, which is the time resolution of the atmospheric transport modelling.

multi-detector site was exposed to the plume through ground deposition a few hours after the explosion. As can be seen, the ground deposition totally dominates the dose rate, however, dose from air exposure will in this case be at a detectable level at a significantly later time (the expected background is on the order of 100 nSv/h). The fact that only ground deposition is observed at early times following the explosion, without any accompanying air activity, is due to particles located above the modelled ground layer (above 300 m) washed down by precipitation, showing up as deposition only in the model. In reality, it is likely that some airborne activity also should be observed, at least by the aerosol station, which is many orders of magnitudes more sensitive (see below).

The stand-alone NaI detector is responding in a similar way as the GM-tube, as shown in figure 39, displaying clearly measured activities of the two fission products ^{99}Mo and ^{140}La, shown as examples of detected nuclides. Again, the detections are caused by ground deposition. The identification of a signal using the NaI-detectors means the nuclear nature of the explosion in this case can be established quickly, only 6 hours after the blast. If some assumptions are made about the nuclide vector, the time evolution of the isotope ratios can additionally be used to estimate the explosion time, making it possible to connect radionuclide observations with possible waveform observations.

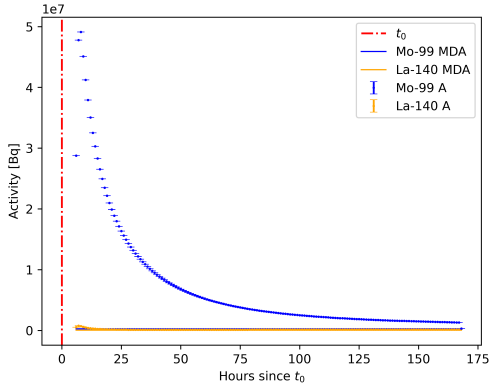

Figure 39: Activity of ROIs dominated by ^{99}Mo and ^{140}La and corresponding minimum detectable activity versus time after explosion A378, as measured by a stand-alone NaI detector. One spectrum is measured and analysed every hour.

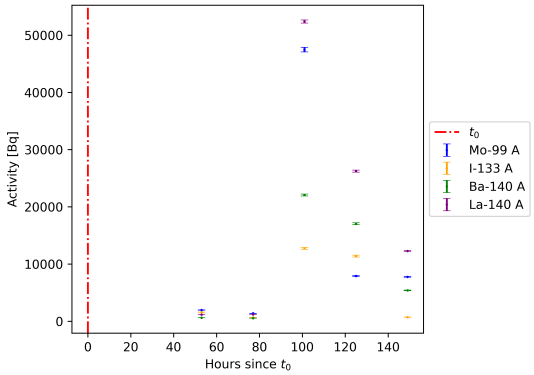

Figure 40: The activity of ^{99}Mo, ^{133}I, ^{140}Ba and ^{140}La as function of time since explosion for explosion A378, as measured by an aerosol system with a HPGe detector. The collection-, decay-, and acquisition times are all 24 hours. Activities are shown at collection start of each sample (but are calculated as mean activities during the entire sampling period of 24 hours).

In contrast to the NaI-detector and the GM-tubes, the aerosol sampling system will only measure modelled airborne activity. Besides release characterization, these measurements are important when estimating inhalation dose. As shown in figure 38, this activity will in this case arrive at the station at later times compared to ground deposition (in this particular case). Consequently, the filters will not show any activity until after around 50 h, as can be seen in the time series in figure 40.

The spectrum of the first filter modelled to contain any activity from explosion A378 is displayed in figure 41, where all identified CTBT-relevant peaks are indicated. A list of all identified CTBT-relevant peaks in this spectrum is shown in table 7.

8.4 Response from noble gas systems

The example network is also equipped with two types of noble gas systems, one SAUNA III with a sample collection time of six hours, and one SAUNA Q_B,

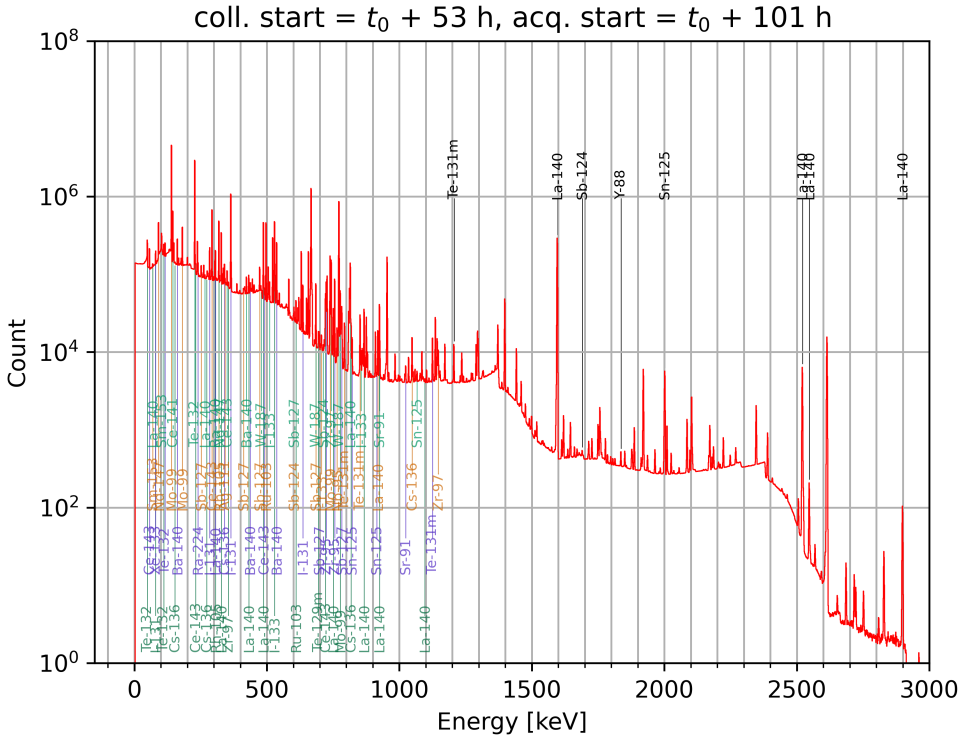

Figure 41: A HPGe energy spectrum collected following explosion A378, as measured in the modelled aerosol system. The acquisition time for the spectrum was 24 hours. Peaks identified by UniSAMPO that are also on the list of CTBT-relevant nuclides are indicated.

Table 7: CTBT-relevant peaks from the energy spectrum in figure 41 identifed by UniSampo. Energies are given in keV.

Energy	Nuclide	Energy	Nuclide	Energy	Nuclide	Energy	Nuclide	Energy	Nuclide
49.5	Te-132	266.5	La-140	473.5	Sb-127	724.4	Zr-95	925.5	Sr-91
57.5	Ce-143	273.4	Cs-136	479.5	W-187	739.4	Mo-99	1024.4	Sr-91
69.5	La-140	284.6	I-131	487.5	La-140	743.4	Zr-97	1048.5	Cs-136
69.5	Sm-153	293.5	Ce-143	490.4	Ce-143	751.4	La-140	1067.2	Sn-125
80.6	I-131	304.5	Ba-140	497.5	Ru-103	756.5	Zr-95	1096.7	La-140
80.6	Xe-133	306.5	La-140	510.6	I-133	765.5	Nb-95	1125.5	Te-131m
91.5	Nd-147	306.5	Rh-105	529.5	I-133	772.5	W-187	1147.5	Zr-97
103.4	Sm-153	319.5	Nd-147	537.5	Ba-140	777.5	Mo-99	1206.5	Te-131m
111.5	Te-132	319.5	Rh-105	603.3	Sb-124	783.2	Sb-127	1596.4	La-140
116.5	Te-132	328.7	La-140	603.3	Sb-127	793.5	Te-131m	1690.4	Sb-124
140.5	Mo-99	340.5	Cs-136	610.5	Ru-103	815.4	La-140	1836.5	Y-88
145.5	Ce-141	342.5	Ag-111	636.5	I-131	818.4	Cs-136	2002.2	Sn-125
153.7	Cs-136	350.5	Ce-143	685.5	Sb-127	822.4	Sn-125	2521.2	La-140
162.5	Ba-140	355.5	Zr-97	685.5	W-187	852.4	Te-131m	2547.2	La-140
181.5	Mo-99	364.5	I-131	695.5	Te-129m	856.4	I-133	2899.2	La-140
228.5	Te-132	412.5	Sb-127	698.3	Sb-127	867.4	La-140		
231.5	Ce-143	423.4	Ba-140	706.5	I-133	915.4	Sn-125		
240.5	Ra-224	432.4	La-140	713.4	Sb-124	919.5	La-140		
252.5	Sb-127	437.5	Ba-140	721.6	Ce-143	925.5	La-140		

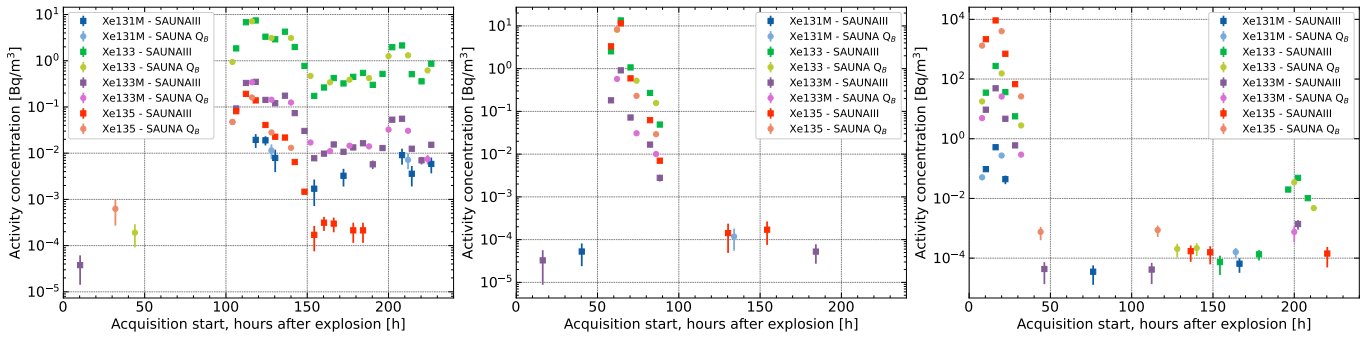

(a) Case A378 (b) Case A421 (c) Case 684

Figure 42: The activity concentration of radioxenon measured by the one station in the test network, for the SAUNA III and SAUNA Q_B instruments. Three example cases are shown; the cases were selected to demonstrate the behaviour at different gas transportation times. Only samples with activity concentrations above the critical detection limit (set a a confidence level of 95%) are shown.

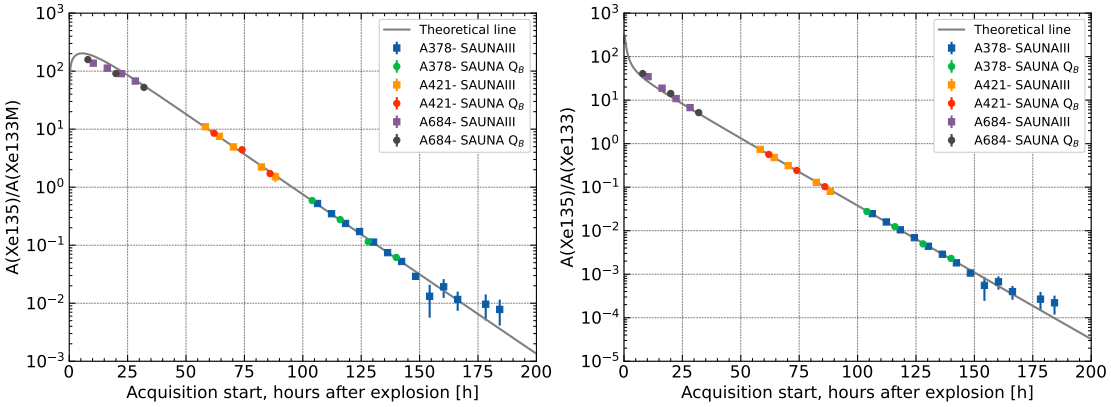

(a) (b)

Figure 43: Ratio of radioxenon with time as measured with SAUNA cube and SAUNAIII, for three picked example cases (A378, A421 and A684). Left plot shows the activity ratio of ^{135}Xe and ^{133m}Xe, the right plot shows the activity ratio of ^{135}Xe and ^{133}Xe, and the gray line is the theoretical values.

with a collection time of 12 hours. Here we use three different explosions from set A (378, 421, and 684) to illustrate data measured at different time delays following an explosion. Measured activity concentration time series for the two systems are displayed in figure 42. As expected, the observed activity concentrations are orders of magnitude higher for the explosion resulting in detections early after the explosion (number 684).

To investigate the validity of the modelling of the sampling-, processing-, and measurement process for noble gas stations, measured activity ratios were plotted and compared to the theoretical values obtained by decaying the nuclide vector. Such plots are shown in figure 43 for the three example explosions. As can be seen, simulated data agrees well with the expected ratio.

This is further illustrated in figure 44, showing a three-ratio isotope plot with simulated data along with the theoretical curve. Plots of this kind is

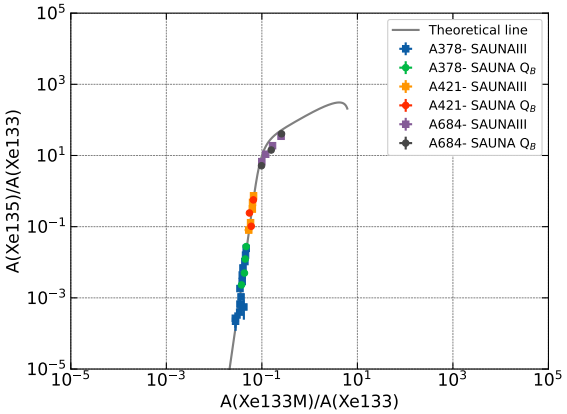

Figure 44: Ratio-ratio plot for radioxenon, for three example cases (A378, A421 and A684), as measured with SAUNA cube and SAUNAIII. The gray line is the theoretical values.

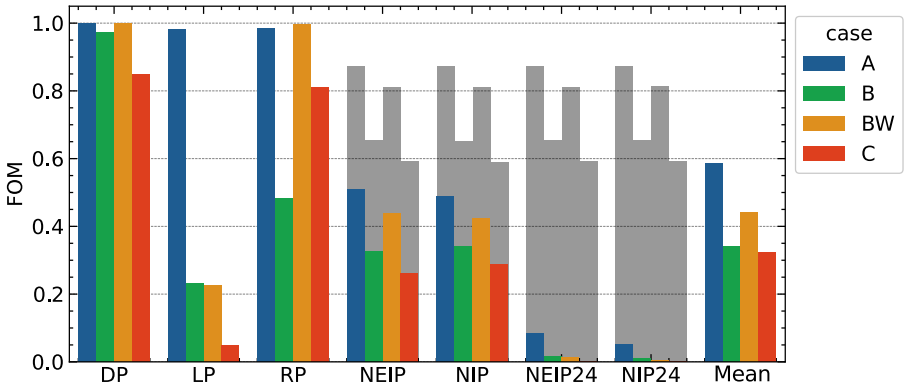

Figure 45: Figure of merits for four different case sets of 1 kt nuclear explosions conducted at an altitude of 150 m, calculated for the network shown in figure 35. The individual FOM measures and the mean of these are shown. DP is detecting power, LP is location power, RP is reporting power, NEIP stands for nuclear explosion identification power, and NIP is nuclide identification power. NEIP24 and NIP24 requires that the conditions are fulfilled within 24 hours. The grey bars in the left figure, for NEIP and NIP, indicates the max total value possible for those measures.

important in order to discriminate releases from nuclear explosions and civil sources, such as emissions from nuclear power plants.

8.5 Figure of merits

Finally, we use the fictious network combined with the response analysis of the explosion sets A, B, BW, and C to illustrate the use of the figure of merits, defined in section 2.4. The calculated figure of merits are shown in figure 45 for the sets A (Sweden), B (Sweden + 700 km, water excluded), BW (Sweden +700 km only water) and C (Europe).

Since the detection power (DP) mainly will be determined by the seismic network, which will have almost 100% efficiency in Sweden and the closest region outside, DP is very close to one for these case sets. Compared to case B, the detection power for case BW is slightly higher. This is caused by the improved seismic coupling for explosions above water. For set C, the detection power is close to 90%, with infrasound contributing to a larger extent than for

the other two cases. The location power (LP), also determined by the waveform technologies, will decrease with increasing sensor-event distance. The reporting power (RP) limit is here set to one hour, and will also decrease for increasing detection distance, limited by the signal travel time for infrasound.

Unlike DP, LP, and RP, the nuclide specific FOMs nuclear explosion identification power (NEIP) and nuclear identification power (NIP), will be heavily affected by the weather conditions (this is also true for infrasound). As shown in section 4.2.4, each case set has a theoretical maximum for the nuclear FOMs, since only a fraction of the calculated releases will reach the Sweden. This maximum is indicated by the grey bars in figure 45. NEIP is calculated using an OR between the two options defined in section 2.4. NEIP and NIP are also calculated with the requirement that the detections and/or nuclide identifications are made within 24 hours (NEIP24 and NIP24). As can be seen in in figure 45, quite a few of the explosions will be identified according to the NIP or NEIP FOM, while very few of these happens within 24 hours.

9 Interactive maps

In addition to the network analysis tools, NEMOS also provides the possibility to produce interactive maps showing results derived from the atmospheric transport calculations, such as deposition fields, as well as measured data from a network of sensors. Furthermore, a functionality to illustrate direct effects, such as dose from initial radiation, is included. The maps are produce using the Python module Folium, and can be viewed in a web browser.

One example is shown in figure 46. The map displays an animation of the dose rate from ground deposition from a nuclear explosion with time, as calculated from the atmospheric dispersion calculations described in section 4. The animation can be played using the control in the lower left corner. Four screen shots of such an animation are shown in figure 47.

The maps also show the position of the sensors in the network. Different sensor types can be selected in a menu. In the example shown in figure 46, the green and red points indicate the positions of sites used as dose rate measurement positions for the local emergency response organisation in Sweden. If the dose rate reaches above 100 nSv/h at any time after the explosion, the position is coloured red.

The calculated dose rate a certain detector position can be viewed by clicking on the corresponding point, as shown in figure 48.

The simulated network in this example also contains the existing aerosol filter stations in Sweden. They are indicated by larger circles, also coloured green or red, depending on if the activities are above detectable levels or not (see figure 46). Since these measurement systems are order of magnitudes more

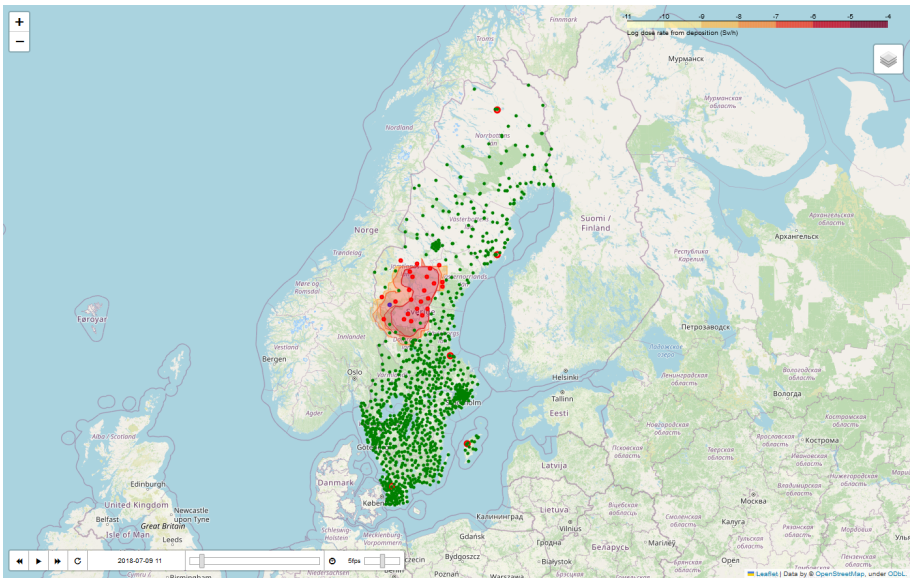

Figure 46: Example of an interactive map showing a sensor network and an animation of the time development of the deposited activity from a nuclear explosion. This example show the measurement positions used by the Swedish emergency response (green and red small circular markers, and aerosol filter stations operated by FOI (larger red and green circles). The colored red area is the calculated dose rate from ground deposition. If the dose rate or activity concentration is above the detection limit, the markers are coloured red.

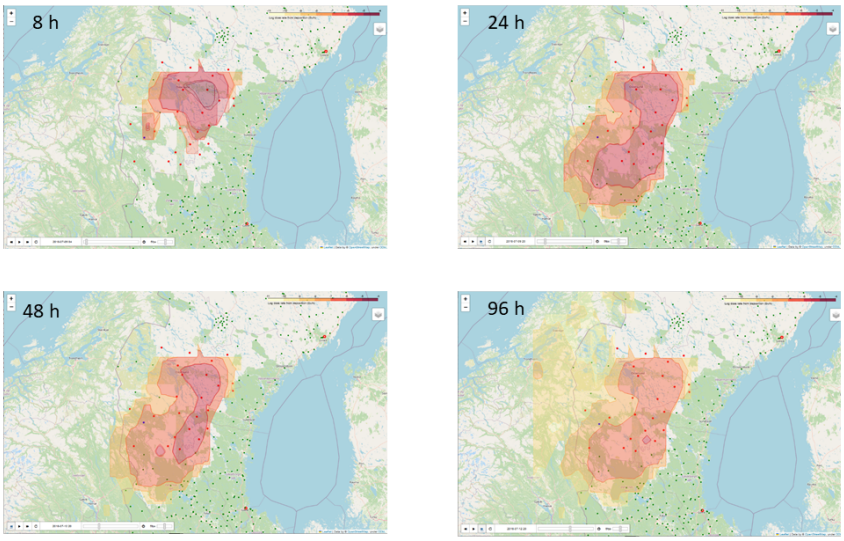

Figure 47: Screen shots showing the animation of the time development of dose rate ffrom ground deposition caused by a 1 kt nuclear explosion detonating 150 m above ground.

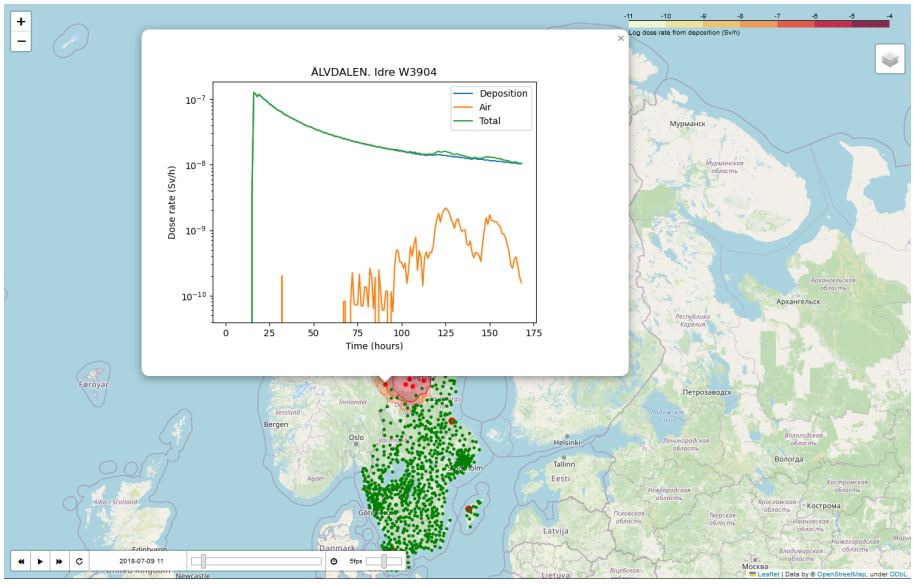

Figure 48: Example of dose rate at a sensor position that can be viewed by mouse clicking on the sensor marker.

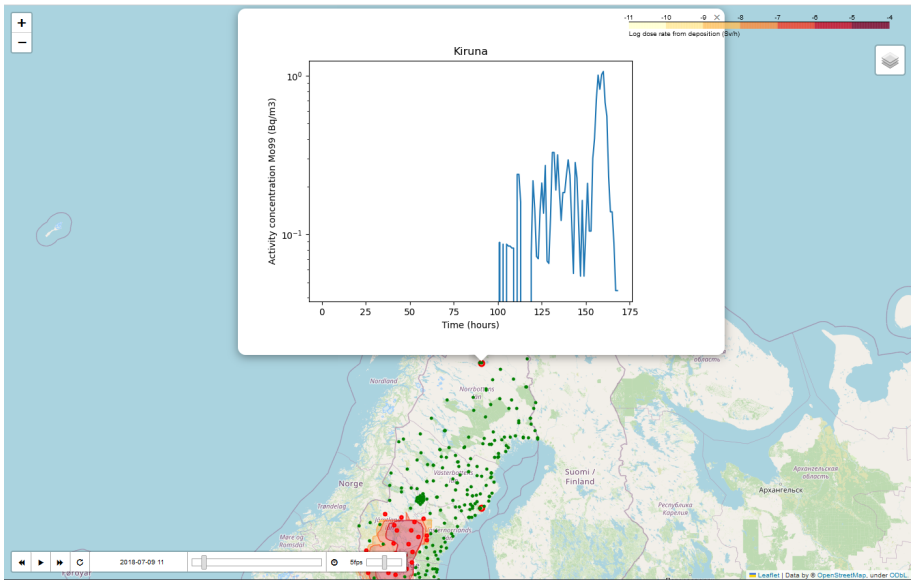

Figure 49: Modelled airborne activity concentration of ^{99}Mo viewed by mouse clicking on an aerosol station.

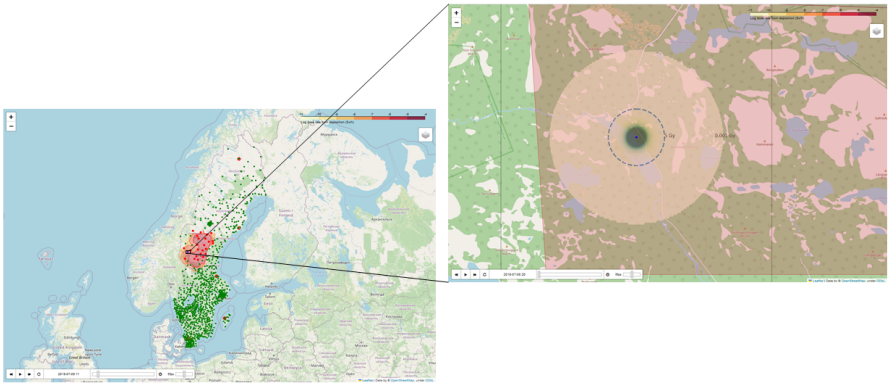

Figure 50: Calculated integrated dose from direct radiation caused by a 1 kt nuclear explosion at a height of 150 m. The dashed circle indicates a dose of 5 Gy, while the outer circle marks the 1 mGy radius.

sensitive than for GM-tubes, they will detect the nuclear fallout at much larger distances. The activity concentration at the sensor position can be inspected, as shown in figure 49.

The interactive maps also provides the possibility to plot direct effects. One example is shown in figure 50, where dose radii from a 1 kt explosion at a height of 150 m is shown.

10 Summary, conclusions and outlook

A software framework (NEMOS) developed to simulate the response of sensor networks, intended to detect, identify, and locate nuclear explosions and other nuclear events, has been developed and is described in this report. The Python-based software simulates the response of sensor networks that can consist of several sub-networks such as a seismic network, an infrasound detection network, and several types of radioactivity sensor networks (GM - tubes measuring dose rate, NaI- sensors measuring isotope-specific activity, either stand-alone or in the vicinity of an air sampling filter, aerosol stations equipped with an HPGe detector, and finally, two types of radioxenon measurement systems).

NEMOS uses a nuclear source vector and atmospheric transport calculations in combination with various detector response models to simulate the radioactivity measurements. A nuclear explosion nuclide vector has been developed that takes into account fission products and neutron activation in weapon material as well as in surrounding media. In the case of HPGe and NaI measurements, a full simulation of measured spectra is performed, and the spectra are analysed with respect to nuclide specific activities and activity concentrations using standard radionuclide analysis software. The responses (detection and location accuracy) of the seismic and infrasound sensors are calculated using empirical models.

A large number of nuclear explosions located in and around Sweden, as well as in Europe, were simulated both with respect to particulate and noble gas dispersion. These explosions can be used in a statistical analysis designed to evaluate different network configurations with respect to verification capability. The analysis include calculation of parameters such as reporting timeliness, detection and location capability, and the capability to identify whether an explosion is nuclear in nature or not.

The framework can also be used to produce interactive maps that show the calculated dispersion fields and which sensors in the network that are detecting the event. The maps can also show detailed measurement data from the individual sensors, as well as illustrations of direct effects. The maps can be used in the planning and excecusion of exercises, as well as in general discussions on nuclear weapons effects.

Although there are room for improvements, in particular in the seismic and infrasound modelling, that use a simplified approach, we believe that the software framework is comprehensive enough to enable a study of the capability of different network configurations that can be of value when designing a measurement network of this kind. The software can also be useful when analysing real measurement data from existing radioactivity measurement networks, since in principle any combination of network and nuclear release can be simulated, with the possibility to include many types of measurement instruments, enabling a comparison with measured and calculated observations.

In the future, the seismic modelling can be made more sophisticated to include local and regional variations, better modelling of location accuracy at larger distances, as well as a more detailed location specific noise model. In addition, the software does not model source location using radionuclide sensors, which normally is performed using backwards atmospheric transport modelling in combination with a source localization method. Another area of improvement is the modelling of the noble gas source term, which should be made to better harmonize with the particle dispersion model. Furthermore, the

algorithm for analysis of NaI spectra should be modified to better correspond to a real spectrum analysis using peak fitting, instead of the simple ROI approach. Another factor not included here is the local radionuclide background. This could be improved by performing actual measurements at potential new sites, and include location-specific numbers in the simulation.

Finally, it should be mentioned that other technologies for nuclear explosion detection exists than the ones included in the model tool described here, as for example discussed in the first report of this project [1]. One example of such a technology is a system for detection of electromagnetic pulses (EMP).

Acknowledgements

Some of the computations and data handling were enabled by resources provided by the National Academic Infrastructure for Supercomputing in Sweden (NAISS) and the Swedish National Infrastructure for Computing (SNIC) at Uppsala Multidisciplinary Center for Advanced Computational Science (UPPMAX) and National Supercomputer Centre (NSC), partially funded by the Swedish Research Council through grant agreements no. 2022-06725 and no. 2018-05973. Anders Axelsson at Swedish Radiation Safety Authority is acknowledged for valuable comments.

Bibliography

[1] Anders Ringbom, Martin Goliath, and Torbjörn Nylén. Ett nationellt system för att uptäcka, varna och informera om kärnexplosioner och andra nukleära händelser. *FOI-R--5465--SE*, June 2023.

[2] L.E. De Geer. CTBT Relevant Radionuclides. Technical Report PTS/IDC-1999/02, 1999.

[3] Per Andersson. Ett datorprogram för beräkning av nuklidvektorer. FOI Internal report - FOI-D–1296–SE., FOI, 2024.

[4] Karl-Heinz Schmidt. http://www.khschmidts-nuclear-web.eu/GEF.html.

[5] D.A. Brown, M.B. Chadwick, R Capote, et al. ENDF/B-VIII.0: the 8th, major release of the nuclear reaction data library with cielo-project cross sections, new standards and thermal scattering data. *Nucl. Data Sheets*, 148:1–142, 2018.

[6] Jeremy Lloyd Conlina, A.C. Kahlerand Austin P. McCartney, and Daniel A. Rehn. Njoy21: Next generation nuclear data processing capabilities. *EPJ Web of Conferences*, 146:09040, 2017.

[7] C.J. Werner et al. MCNP6.2 Release Notes. Technical Report LA-UR-18-20808, Los Alamos National Laboratory, 2018.

[8] Peder Kock Anders Axelsson, Jan Johansson, Jonas Lindgren, Anna Maria Blixt Buhr, Jonas Boson, Ulf Bäverstam, and Simon Karlsson. Radiological Consequences of Fallout from Nuclear Explosions. *SSM Report*, 2023:05e, 2023.

[9] Annika Tovedal, Martin Goliath, Petra Lagerkvist, and Torbjörn Nylén. Approximativa källtermer för kärnladdningsexplosioner. *FOI Memo 7177*, July 2020.

[10] Ted Harvey, F Serduke, L Edwards, and L Peters. Kdfoc3: A nuclear fallout assessment capability. *UCRL-52338, Lawrence Livermore National Laboratory*, 1992.

[11] A. F. Stein, R. R. Draxler, G. D. Rolph, B. J. B. Stunder, M. D. Cohen, and F. Ngan. NOAA's HYSPLIT Atmospheric Transport and Dispersion Modeling System. *Bulletin of the American Meteorological Society*, 96(12):2059 – 2077, 2015.

[12] P. von Schoenberg, D. Elfverson, L. Persson, and D. Vågberg. Nwswamp manual, version 1.4. Report, Swedish Defence Research Agency, 2024.

[13] J. Lindqvist. En stokastisk partikelmodel i ett ickemetriskt koordinatsystem. Report FOA R –99-01086-862–SE, Swedish Defence Research Agency, 1999.

[14] D. Elfverson and D. Vågberg. Deposition of radioactive particles in depello. Report FOI Memo 8147, 2023.

[15] Henrik Grythe, Nina I Kristiansen, Christine D Groot Zwaaftink, Sabine Eckhardt, Johan Ström, Peter Tunved, Radovan Krejci, and Andreas Stohl. A new aerosol wet removal scheme for the lagrangian particle model flexpart v10. *Geoscientific Model Development*, 10(4):1447–1466, 2017.

[16] John H Seinfeld and Spyros N Pandis. From air pollution to climate change. *Atmospheric chemistry and physics*, 1326, 1998.

[17] Leiming Zhang, Sunling Gong, Jacob Padro, and Len Barrie. A size-segregated particle dry deposition scheme for an atmospheric aerosol module. *Atmospheric environment*, 35(3):549–560, 2001.

[18] NOAA Air Recources Laboratory. Gridded Meteorological Data Archives, 2023.

[19] Ernest Rutherford, Ernest Rutherford, and J. and C. F. Clay. *Radioactivity*. At the University Press, Cambridge, 1904.

[20] Bateman. The solution of a system of differential equations occurring in the theory of radioactive transformations. *Proc. Cambridge Philos. Soc.*, 15:423–427, 1910.

[21] Eric Jones, Travis Oliphant, Pearu Peterson, et al. SciPy: Open source scientific tools for Python, 2001–.

[22] N. Petoussi-Henss, D. Satoh, A. Endo, K.F. Eckerman, W.E. Bolch, J. Hunt, J.T.M. Jansen, C.H. Kim, C. Lee, K. Saito, H. Schlattl, Y.S. Yeom, and S.J. Yoo. Icrp publication 144: Dose coefficients for external exposures to environmental sources. *Annals of the ICRP*, 49(2):11–145, 2020. PMID: 33115250.

[23] J. Kastlander and C. Söderström. Evaluation of an early warning system for airborne radionuclides. *Applied Radiation and Isotopes*, 126:228–231, 2017. Proceedings of the 7th International Conference on Radionuclide Metrology – Low-Level Radioactivity Measurement Techniques.

[24] S. Agostinelli, J. Allison, K. Amako, J. Apostolakis, H. Araujo, P. Arce, M. Asai, D. Axen, S. Banerjee, G. Barrand, F. Behner, L. Bellagamba, J. Boudreau, L. Broglia, A. Brunengo, H. Burkhardt, S. Chauvie, J. Chuma, R. Chytracek, G. Cooperman, G. Cosmo, P. Degtyarenko, A. Dell'Acqua, G. Depaola, D. Dietrich, R. Enami, A. Feliciello, C. Ferguson, H. Fesefeldt, G. Folger, F. Foppiano, A. Forti, S. Garelli, S. Giani, R. Giannitrapani, D. Gibin, J.J. Gómez Cadenas, I. González, G. Gracia Abril, G. Greeniaus, W. Greiner, V. Grichine, A. Grossheim, S. Guatelli, P. Gumplinger, R. Hamatsu, K. Hashimoto, H. Hasui, A. Heikkinen, A. Howard, V. Ivanchenko, A. Johnson, F.W. Jones, J. Kallenbach, N. Kanaya, M. Kawabata, Y. Kawabata, M. Kawaguti, S. Kelner, P. Kent, A. Kimura, T. Kodama, R. Kokoulin, M. Kossov, H. Kurashige, E. Lamanna, T. Lampén, V. Lara, V. Lefebure, F. Lei, M. Liendl, W. Lockman, F. Longo, S. Magni, M. Maire, E. Medernach, K. Minamimoto, P. Mora de Freitas, Y. Morita, K. Murakami, M. Nagamatu, R. Nartallo, P. Nieminen, T. Nishimura, K. Ohtsubo, M. Okamura, S. O'Neale, Y. Oohata, K. Paech, J. Perl, A. Pfeiffer, M.G. Pia, F. Ranjard, A. Rybin, S. Sadilov, E. Di Salvo, G. Santin, T. Sasaki, N. Savvas, Y. Sawada, S. Scherer, S. Sei, V. Sirotenko, D. Smith, N. Starkov, H. Stoecker, J. Sulkimo, M. Takahata, S. Tanaka, E. Tcherniaev, E. Safai Tehrani, M. Tropeano, P. Truscott, H. Uno, L. Urban, P. Urban, M. Verderi, A. Walkden, W. Wander, H. Weber, J.P. Wellisch, T. Wenaus, D.C. Williams, D. Wright, T. Yamada, H. Yoshida, and D. Zschiesche. Geant4—a simulation toolkit. *Nuclear Instruments and Methods in Physics Research Section A: Accelerators, Spectrometers, Detectors and Associated Equipment*, 506(3):250–303, 2003.

[25] J. Allison, K. Amako, J. Apostolakis, H. Araujo, P. Arce Dubois, M. Asai, G. Barrand, R. Capra, S. Chauvie, R. Chytracek, G.A.P. Cirrone, G. Cooperman, G. Cosmo, G. Cuttone, G.G. Daquino, M. Donszelmann, M. Dressel, G. Folger, F. Foppiano, J. Generowicz, V. Grichine, S. Guatelli, P. Gumplinger, A. Heikkinen, I. Hrivnacova, A. Howard, S. Incerti, V. Ivanchenko, T. Johnson, F. Jones, T. Koi, R. Kokoulin, M. Kossov, H. Kurashige, V. Lara, S. Larsson, F. Lei, O. Link, F. Longo, M. Maire, A. Mantero, B. Mascialino, I. McLaren, P. Mendez Lorenzo, K. Minamimoto, K. Murakami, P. Nieminen, L. Pandola, S. Parlati, L. Peralta, J. Perl, A. Pfeiffer, M.G. Pia, A. Ribon, P. Rodrigues, G. Russo, S. Sadilov, G. Santin, T. Sasaki, D. Smith, N. Starkov, S. Tanaka, E. Tcherniaev, B. Tome, A. Trindade, P. Truscott, L. Urban, M. Verderi, A. Walkden, J.P. Wellisch, D.C. Williams, D. Wright, and H. Yoshida. Geant4 developments and applications. *IEEE Transactions on Nuclear Science*, 53(1):270–278, 2006.

[26] J. Allison, K. Amako, J. Apostolakis, P. Arce, M. Asai, T. Aso, E. Bagli, A. Bagulya, S. Banerjee, G. Barrand, B.R. Beck, A.G. Bogdanov, D. Brandt, J.M.C. Brown, H. Burkhardt, Ph. Canal, D. Cano-Ott, S. Chauvie, K. Cho, G.A.P. Cirrone, G. Cooperman, M.A. Cortés-Giraldo, G. Cosmo, G. Cuttone, G. Depaola, L. Desorgher, X. Dong, A. Dotti, V.D. Elvira, G. Folger, Z. Francis, A. Galoyan, L. Garnier, M. Gayer, K.L. Genser, V.M. Grichine, S. Guatelli, P. Guèye, P. Gumplinger, A.S. Howard, I. Hřivnáčová, S. Hwang, S. Incerti, A. Ivanchenko, V.N. Ivanchenko, F.W. Jones, S.Y. Jun, P. Kaitaniemi, N. Karakatsanis, M. Karamitros, M. Kelsey, A. Kimura, T. Koi, H. Kurashige, A. Lechner, S.B. Lee, F. Longo, M. Maire, D. Mancusi, A. Mantero, E. Mendoza, B. Morgan, K. Murakami, T. Nikitina, L. Pandola, P. Paprocki, J. Perl, I. Petrović, M.G. Pia, W. Pokorski, J.M. Quesada, M. Raine, M.A. Reis, A. Ribon, A. Ristić Fira, F. Romano, G. Russo, G. Santin, T. Sasaki, D. Sawkey, J.I. Shin, I.I. Strakovsky, A. Taborda, S. Tanaka, B. Tomé, T. Toshito, H.N. Tran, P.R. Truscott, L. Urban, V. Uzhinsky, J.M. Verbeke, M. Verderi, B.L. Wendt, H. Wenzel, D.H. Wright, D.M. Wright, T. Yamashita, J. Yarba, and H. Yoshida. Recent developments in geant4. *Nuclear Instruments and Methods in Physics Research Section A: Accelerators, Spectrometers, Detectors and Associated Equipment*, 835:186–225, 2016.

[27] D.A. Brown, M.B. Chadwick, R. Capote, A.C. Kahler, A. Trkov, M.W. Herman, A.A. Sonzogni, Y. Danon, A.D. Carlson, M. Dunn, D.L. Smith, G.M. Hale, G. Arbanas, R. Arcilla, C.R. Bates, B. Beck, B. Becker, F. Brown, R.J. Casperson, J. Conlin, D.E. Cullen, M.-A. Descalle, R. Firestone, T. Gaines, K.H. Guber, A.I. Hawari, J. Holmes, T.D. Johnson, T. Kawano, B.C. Kiedrowski, A.J. Koning, S. Kopecky, L. Leal, J.P. Lestone, C. Lubitz, J.I. Márquez Damián, C.M. Mattoon, E.A. McCutchan, S. Mughabghab, P. Navratil, D. Neudecker, G.P.A. Nobre, G. Noguere, M. Paris, M.T. Pigni, A.J. Plompen, B. Pritychenko, V.G. Pronyaev, D. Roubtsov, D. Rochman, P. Romano, P. Schillebeeckx, S. Simakov, M. Sin, I. Sirakov, B. Sleaford, V. Sobes, E.S. Soukhovitskii, I. Stetcu, P. Talou, I. Thompson, S. van der Marck, L. Welser-Sherrill, D. Wiarda, M. White, J.L. Wormald, R.Q. Wright, M. Zerkle, G. Žerovnik, and Y. Zhu. ENDF/B-VIII.0: The 8th Major Release of the Nuclear Reaction Data Library with CIELO-project Cross Sections, New Standards and Thermal Scattering Data. *Nuclear Data Sheets*, 148:1–142, 2018. Special Issue on Nuclear Reaction Data.

[28] L. A. Currie. Limits for Qualitative Detection and Quantitative Determination. *Analytical Chemistry*, 40, 1968.

[29] Glenn .F. Knoll. *Radiation Detection and Measurement.* Wiley, 4th edition, 2010.

[30] J. Kastlander and C. Söderström. Tidig varning-system vid de nationella luftfilterstationerna. Technical Report FOI-R–3581–SE, FOI, December 2012.

[31] Szymon Guguła, Krzysztof Kozak, Jadwiga Mazur, Dominik Grządziel, and Mariusz Mroczek. Fast in situ gamma spectroscopy using handheld spectrometer with nai probe. *Journal of Environmental Radioactivity*, 188:87–94, 2018. 7th International Symposium on IN SItu NUclear MEtrology as a tool for radioecology – INSINUME- 2017.

[32] Ingemar Vintersved and Lars-Erik De Geer. The Swedish Air Monitoring Network for Particulate Radioactivity. *IEEE Transactions on Nuclear Science*, 29(1):827–831, 1982.

[33] R. Plenteda. *A Monte Carlo based virtual gamma spectroscopy laboratory.* PhD thesis, Technische Univ. Wien, Wien (Austria), June 2002.

[34] Formats and Protocols for Messages. Specification ID-C/ENG/SPC/103/Rev.7, Preparatory Commission for the Comprehensive Nuclear-Test-Ban Treaty Organization (CTBTO), 2016.

[35] P.A. Aarnio, J.J. Ala-Heikkilä, and T.T. Hakulinen. Performance of UNISAMPO-SHAMAN with gamma-ray spectra containing known traces of fission products. *J. Radioanal. Nucl. Chem.*, 276:455–460, May 2008.

[36] Mattias Aldener, Anders Axelsson, Tomas Fritioff, Johan Kastlander, and Anders Ringbom. SAUNA III - The next generation noble gas system for verification of nuclear explosions. *Journal of Environmental Radioactivity*, 262:107159, 2023.

[37] Anders Ringbom, Tomas Fritioff, Mattias Aldener, Anders Axelsson, Klas Elmgren, Carl Hellesen, Lindsay Karlkvist, Johan Kastlander, Henrik Olsson, Helena Berglund, Bo Hellman, and Ola Pettersson. SAUNA Q_B - Array: The realization of a new concept in radioxenon detection. *Journal of Environmental Radioactivity*, 261:107136, 2023.

[38] M W Edenburn, M L Bunting, and A C Payne, Jr. CTBT Integrated Verification System Evaluation Model. *SANDIA report SAND-97-2518*, 1997.

[39] Peter J. Gaebler and Lars Ceranna. Performance of the International Monitoring System Seismic Network Based on Ambient Seismic Noise Measurements. *Pure and Applied Geophysics*, 178(7):2419–2436, 2022.

[40] Jr. Sereno, Thomas J, Steven R Bratt, and Gaymond Yee. NETSIM: A Computer Program for Simulating Detection and Location Capability of Regional Seismic Networks. *SCIENCE APPLICATIONS INTERNATIONAL CORP SAN DIEGO CA, Annual technical rept. no1, 1 Jan 1989 - 1 Jan 1990.*

[41] Frode Ringdal, Peter D. Marshall, and Ralph W. Alewine. Seismic yield determination of Soviet underground nuclear explosions at the Shagan River test site. *Geophysical Journal International*, 109(1):65–77, 04 1992.

[42] *"IDC Processing of Seismic, Hydroacoustic and Infrasonic Data"*. IDC/OPS/MAN/001/Rev.3, May 2022.

[43] B. L. N. Kennett and E. R. Engdahl. Traveltimes for global earthquake location and phase identification. *Geophysical Journal International*, 105(2):429–465, 05 1991.

[44] Björn Lund, Peter Schmidt, Zaher Hossein Shomali, and Michael Roth. The Modern Swedish National Seismic Network: Two Decades of Intraplate Microseismic Observation. *Seismological Research Letters*, 92(3):1747–1758, 03 2021.

[45] Helmholtz-Centre Potsdam - GFZ German Research Centre for Geosciences and gempa GmbH. The SeisComP seismological software package. GFZ Data Services., 2008.

[46] S.R. Bratt and W. Nagy. The LocSAT Program. Science Applications International Corporation (SAIC), San Diego, 1991.

[47] Karl Koch and Christoph Pilger. Infrasound observations from the site of past underground nuclear explosions in North Korea. *Geophysical Journal International*, 216(1):182–200, 09 2018.

[48] J. P. Mutschlecner and R. W. Whitaker. The Correction of Infrasound Signals for Upper Atmospheric Winds. Fourth International Symposium on Long Range Sound Propagation, ASA Cp-3101, 1990.

[49] Global Modeling and Assimilation Office (GMAO) (2015), MERRA-2 instM_3d_ana_Np: 3d,Monthly mean,Instantaneous,Pressure-Level,Analysis,Analyzed Meteorological Fields V5.12.4, Greenbelt, MD, USA, Goddard Earth Sciences Data and Information Services Center (GES DISC), Accessed: 2023-11-15 at doi:10.5067/V92O8XZ30XBI.

[50] Global Modeling and Assimilation Office (GMAO) (2015), MERRA-2 tavgM_2d_flx_Nx: 2d,Monthly mean,Time-Averaged,Single-Level,Assimilation,Surface Flux Diagnostics V5.12.4, Greenbelt, MD, USA, Goddard Earth Sciences Data and Information Services Center (GES DISC), Accessed: 2023-11-27 at doi: 10.5067/0JRLVL8YV2Y4.

FOI
Defence Research Agency
SE-164 90 Stockholm

Phone: +46 8 555 030 00
Fax: +46 8 555 031 00

www.foi.se